

The Spectra of IceCube Neutrino (SIN) candidate sources - IV. Spectral energy distributions and multi-wavelength variability

Martina Karl^{1,2*}, Paolo Padovani^{2,3}, Paolo Giommi^{4,5,6}

¹Technische Universität München, TUM School of Natural Sciences, Physics Department, James-Frank-Str. 1, D-85748 Garching bei München, Germany

²European Southern Observatory, Karl-Schwarzschild-Str. 2, D-85748 Garching bei München, Germany

³Associated to INAF - Osservatorio di Astrofisica e Scienza dello Spazio, Via Piero Gobetti 93/3, I-40129 Bologna, Italy

⁴Institute for Advanced Study, Technische Universität München, Lichtenbergstrasse 2a, D-85748 Garching bei München, Germany

⁵Center for Astro, Particle and Planetary Physics (CAP3), New York University Abu Dhabi, PO Box 129188 Abu Dhabi, United Arab Emirates

⁶Associated to INAF, Osservatorio Astronomico di Brera, via Brera, 28, I-20121 Milano, Italy

Accepted XX. Received YY; in original form ZZ

ABSTRACT

We present hybrid spectral energy distributions, combining photon and neutrino fluxes, for a sample of blazars, which are candidate IceCube neutrino sources. We furthermore check for differences in our sources' variability in the near-infrared, optical, X-ray and γ -ray bands compared to a sample of non-neutrino source candidate blazars, and investigate the state of each blazar at the arrival time of high-energy neutrinos. We find no significant differences when comparing our sample with control sources, also in terms of their spectral energy distributions, and no correlation between flaring states and neutrino arrival times. Looking for signatures of hadronic production, we check for similar strengths of the γ -ray and neutrino fluxes and find a 2.2σ signal for our source candidates. The hybrid spectral energy distributions assembled here will form the basis of the next step of our project, namely lepto-hadronic modelling of these blazars to assess the physical likelihood of a neutrino connection.

Key words: neutrinos — radiation mechanisms: non-thermal — galaxies: active — BL Lacertae objects: general — gamma-rays: galaxies — astroparticle physics

1 INTRODUCTION

Ten years ago the IceCube Neutrino Observatory¹ detected the first high-energy astrophysical neutrinos of likely extragalactic origin with energies reaching more than 1 PeV (10^{15} eV; IceCube Collaboration 2013) and since then has produced a growing list of events (e.g. Abbasi et al. 2022a, and references therein). So far, however, only two extragalactic objects have been associated with a significance larger than $\sim 3\sigma$ with IceCube neutrinos. Namely, the blazar TXS 0506+056 at $z = 0.3365$ (at the $3 - 3.5\sigma$ level: IceCube Collaboration et al. 2018b,a) and the local ($z = 0.004$) Seyfert 2 galaxy NGC 1068 (at the 4.2σ level: Abbasi et al. 2022b) (see also Giommi & Padovani 2021 for a recent review on possible astronomical associations).

Giommi et al. (2020, hereafter G20) carried out a detailed dissection of all the public IceCube high-energy neutrinos that were well reconstructed (so-called tracks) and off the Galactic plane at the time of publication, which provided a 3.2σ (post-trial) correlation

excess with γ -ray detected IBLs² and HBLs. No excess was found for LBLs. Based on these results, out of the 47 IBLs and HBLs in Table 5 of G20 16 ± 4 could be new neutrino sources waiting to be identified.

To test this out, we required optical spectra, needed to measure the redshift, which were not available for the majority of the G20 sample, and hence derive the luminosity of the source, vital to do any modelling, determine the properties of the spectral lines, and also possibly estimate the mass of the central black hole, M_{BH} .

Our group has therefore started “The spectra of IceCube Neutrino (SIN) candidate sources” project, whose main aims are to: (1) conduct an observational campaign to secure optical spectra; (2) determine the nature of the sources; (3) assemble their SEDs using all available multi-wavelength and neutrino data; (4) model their SEDs and, subsequently, the expected neutrino emission from

² Blazars are sub-divided from a spectral energy distribution (SED) point of view on the basis of the rest-frame frequency of their low-energy (synchrotron) hump ($\nu_{\text{peak}}^{\text{S}}$) into low- (LBL/LSP: $\nu_{\text{peak}}^{\text{S}} < 10^{14}$ Hz [< 0.41 eV]), intermediate- (IBL/ISP: 10^{14} Hz $< \nu_{\text{peak}}^{\text{S}} < 10^{15}$ Hz [$0.41 - 4.1$ eV]), and high-energy (HBL/HSP: $\nu_{\text{peak}}^{\text{S}} > 10^{15}$ Hz [> 4.1 eV]) peaked sources respectively (Padovani & Giommi 1995; Abdo et al. 2010).

* E-mail: martina.karl@eso.org

¹ <http://icecube.wisc.edu>

each blazar; (5) determine the likelihood of a connection between the neutrino and the blazar using a physical model for the blazar multi-messenger emissions, as done, for example, by some of us in [Petrovoulou et al. \(2015, 2020\)](#).

We have addressed point (1) in [Paiano et al. \(2021, hereafter Paper I\)](#) and [Paiano et al. \(2023, hereafter Paper III\)](#), who presented the spectroscopy of a large fraction of the objects selected by G20, which, together with results taken from the literature, covered the whole sample³. Point (2) was dealt with in [Padovani et al. \(2022, hereafter Paper II\)](#) and Paper III, where it was shown that the BL Lacs under study were, in many cases (34 – 77 per cent), masquerading BL Lacs, i.e. objects in which the weakness of the emission lines and their low values of the equivalent widths were due to a very bright Doppler-boosted continuum, which was washing out the lines, unlike “real” BL Lacs, which are intrinsically weak-lined objects. As discussed in Papers II and III, this is extremely important for two reasons: (1) “real” BL Lacs and FSRQs turn out to belong to two very different physical classes, i.e. objects without and with high-excitation emission lines in their optical spectra, referred to as low-excitation (LEGs) and high-excitation galaxies (HEGs), respectively (e.g. [Padovani et al. 2017](#), and references therein); (2) masquerading BL Lacs, being HEGs, benefit from several radiation fields external to the jet (i.e. the accretion disc, photons reprocessed in the broad-line region (BLR) or from the dusty torus), which, by providing more targets for the protons, might enhance neutrino production as compared to LEGs. Indeed TXS 0506+056, which is the blazar with the most significant association with a neutrino event ([IceCube Collaboration et al. 2018b,a](#)) is also a masquerading BL Lac ([Padovani et al. 2019](#)).

The purpose of this paper is to take care of point (3), that is, collect all available multi-wavelength and neutrino data for the G20 sources and put together their hybrid SEDs. Given the amount of available data, we also study our sources’ variability in the near-infrared (IR), optical, X-ray, and γ -ray bands to see how they behave compared to the rest of the blazar population, and check if there are any electromagnetic flares in these bands coincident with the neutrino arrival times.

The paper is structured as follows: Section 2 presents updates to the G20 sources, in Section 3 and 4 we describe the multi-messenger (photon and neutrino) data that we have used in this paper, while Section 5 presents the results of the SEDs, the variability properties in the various bands, and searches for flares coincident with neutrinos. Finally, Section 6 discusses our results, and Section 7 summarises our conclusions. Appendix A provides complementary information. We use a Λ CDM concordance cosmology with Hubble constant $H_0 = 70 \text{ km s}^{-1} \text{ Mpc}^{-1}$, matter density $\Omega_{m,0} = 0.3$, and dark energy density $\Omega_{\Lambda,0} = 0.7$.

2 AN UPDATE TO RECENT ICECUBE TRACKS

Since 2019 the IceCube collaboration has revised the criteria for identifying neutrino events with a probable astrophysical origin ([Blaufuss et al. 2019; Abbasi et al. 2023](#)). They also introduced different classifications of tracks, differentiating between “gold” and “bronze” alerts. Gold alerts aim for a higher astrophysical purity compared to bronze alerts. The previous selection criteria for the tracks in G20 are mostly comparable to the gold stream. Based on

[Abbasi et al. \(2023\)](#), we identified which G20 sources no longer belong to the updated high-energy neutrino event selection⁴ and list them in the bottom section of Table 1. This leaves 34 out of 49 G20 sources for this paper’s analysis. However, we also present the multi-messenger SEDs of the fifteen excluded sources since they were already assembled when the new selection was published.

We note that the original selection for the G20 sample included $\nu_{\text{peak}}^S > 10^{14} \text{ Hz}$. As described in the G20 paper, ν_{peak}^S values were derived by first removing all data points that could be attributed to components unrelated to the jet synchrotron emission, namely the host galaxy (usually in the IR and optical bands), the blue bump (blue + UV), and inverse Compton emission (X-ray). The remaining data were then fitted with a 2nd-order polynomial using the SSDC–SED tool⁵. We have re-estimated ν_{peak}^S for all our sources as done for the control sample (where applicable) using BlaST ([Glauch et al. 2022](#)) after retrieving the SEDs for each of these blazars with VOU-Blazars V1.96 ([Chang et al. 2020](#)). The average logarithmic difference between the G20 ν_{peak}^S and BlaST ν_{peak}^S is 0.2 ± 0.1 . This is within the mean uncertainty of the BlaST $\log \nu_{\text{peak}}^S = 0.54 \pm 0.02$. As a result, and because now we also have more data available compared to G20, some sources turned out to have $\nu_{\text{peak}}^S < 10^{14} \text{ Hz}$. However, we follow [Giommi & Padovani \(2021\)](#) and consider only IHBLs, i.e., sources with rest-frame (i.e., multiplied by $[1+z]$) $\nu_{\text{peak}}^S \geq 10^{13.5} \text{ Hz}$ (within their uncertainties), which means no source gets excluded due to their ν_{peak}^S . Tab. 1 lists the current sample, their rest-frame ν_{peak}^S , and the sources excluded because of the revised IceCube selection criteria.

3 PHOTON DATA

3.1 Multi-wavelength SEDs

We obtain the multi-frequency data with VOU-Blazars, which queries many different catalogues (listed in Appendix A) providing flux measurements across a wide range of the electromagnetic spectrum. TeV data for two sources (3HSP J023248.5+20171, a.k.a. 1ES 0229+200, and TXS 0506+056) were added by hand ([IceCube Collaboration et al. 2018b; Costamante et al. 2018](#)).

For the γ -ray band, we use data from the *Fermi* large area telescope (*Fermi*-LAT: [Ackermann et al. 2012](#)) from August 2008 to August 2022 as available. We use the python package Fermipy ([Wood et al. 2017](#)) for the analysis. We apply the recommended selections for an off-plane point source analysis⁶ for Pass 8 data (P8R3). This includes filtering for photons (evclass = 128, evtype = 3) with energies 0.1 – 100 GeV within a radius of 9° around the source. Furthermore, we remove Earth limb contamination by requiring a zenith angle $\leq 90^\circ$ and requiring good data quality ((DATA_QUAL > 0) and (LAT_CONFIG = 1)). The procedures for the preparation of the data are described in the *Fermi* Cicerone⁷.

After selecting the data, we define the model in the following

⁴ Tracks previously used by G20 but no longer included in the revised IceCube event list are IC160331A, IC141109A, IC150428A, IC141209A, IC141126A, IC120123A, IC140216A, IC170506A, IC190104A.

⁵ <https://tools.ssdc.asi.it/SED/>

⁶ https://fermi.gsfc.nasa.gov/ssc/data/analysis/documentation/Cicerone/Cicerone_Data_Exploration/Data_preparation.html

⁷ <https://fermi.gsfc.nasa.gov/ssc/data/analysis/documentation/Cicerone/>

³ To the G20 sample we further added M87 and 3HSP J095507.9+35510, for reasons described in Paper II, for a total of 49 sources.

way. The background hypothesis comprises known sources within a radius of 95 per cent of the point spread function, the diffuse galactic and the diffuse isotropic γ -ray background. The signal hypothesis is the background scenario with an additional signal by a point source at the centre. We assume a signal emission following a power law in most cases, unless a log-parabola is a better fit. The test statistic is the ratio of the maximised background likelihood $\mathcal{L}_{\max,0}$ versus the maximised signal likelihood $\mathcal{L}_{\max,1}$: $\text{TS} = -2 \ln (\mathcal{L}_{\max,0} / \mathcal{L}_{\max,1})$. A larger TS value indicates that the background hypothesis can be rejected. The best-fit parameters for the central point source are then plotted in the SED. We provide the output of the fits in a GitHub repository⁸.

3.2 Variability study

For the variability study of blazars, we collect data in the IR, optical, X-ray, and γ -ray bands. By construction, all the candidate neutrino blazars in the G20 sample are also γ -ray sources. Therefore, the natural control sample is the set of blazars in the 4LAC-DR3 catalogue (Ajello et al. 2020; Lott et al. 2020). We consider all objects classified as blazars (FSRQs, BL Lacs, and BCUs) without entries in the analysis flag (other than 0). Since the redshift is not known for all background blazars, we use the observed ν_{peak}^S (and not the rest-frame one) when binning for the variability analysis for both the background and the G20 samples. We also apply the $\nu_{\text{peak}}^S \geq 10^{13.5}$ Hz cut to the *observed* values to both samples, as this is a good value to separate LBLs from IHBL blazars (e.g. Giommi & Padovani 2021). This removes three sources (5BZU J0158+0101, CRATESJ024445+132002, and CRATESJ232625+011147) from our sample and leaves us with 31 sources for the variability study when binning in ν_{peak}^S for the comparison to the background sample. We note that these three sources still meet the ν_{peak}^S criterion within their uncertainties when considering their rest-frame ν_{peak}^S . Table A1 lists the time span covered and the sampling of the light curves used to calculate the FVs in the IR, optical, and X-ray bands.

3.2.1 IR band

The intermediate location of IR wavelengths within the overall SED is particularly beneficial for blazar studies since the spectral slope in this energy band is a direct measurement of whether ν_{peak}^S is located at frequencies $\lesssim 10^{13}$ Hz, like in LBL sources, or $\gtrsim 10^{13.5}$ Hz, like in the case of IBL and HBL blazars. The amount of IR variability over time is also useful in quantifying the dynamics of the multi-frequency emission in blazars.

The WISE satellite (Wright et al. 2010) observed the entire sky at IR frequencies during its main mission in 2010 and as part of the NEOWISE reactivation phase (Mainzer et al. 2014), which started in 2013 and is still ongoing. Although the main purpose of NEOWISE is to track near-Earth objects, it also detected a large number of blazars at two infrared wavelengths (3.4 and 4.6 μm), generating a very valuable blazar variability database covering a period of over nine years.

We found WISE and NEOWISE data for 47 out of the original 49 sources using the VOU-Blazars tool (Chang et al. 2020) V1.96. After removing sources as described above, we have 30 sources with IR data left. Furthermore, we retrieved WISE and NEOWISE data

for the control sample in the 4LAC-DR3 catalogue with $\nu_{\text{peak}}^S \geq 10^{13.5}$ Hz, i.e., 1479 blazars.

3.2.2 Optical band

Whenever possible, we retrieved flux measurements from the Zwicky Transient Facility (ZTF: Bellm et al. 2019). This sky monitoring survey offers magnitudes measurements with a three-day cadence in three optical filters for astronomical sources at $\delta \gtrsim -30^\circ$.

We generated optical light curves with data from the ZTF for the G20 sources and the blazars in the 4LAC-DR3 catalogue falling within the sampled declination range, deriving results for 43 out of the original sample of 49 G20 sources. After applying the updated criteria as described above, we have 29 optical light curves and fractional variabilities (FVs; see equation 1). The background sample consists of 1135 blazars.

3.2.3 X-ray band

Swift-XRT⁹ observations are available for 37 of the 49 G20 sources. Of these, 17 sources have sufficient measurements to calculate the FV. After cleaning the sample as described above, eleven sources remain. As for the control sample, most 4LAC-DR3 blazars have not been observed multiple times in the X-ray band. Hence, only for the X-ray band, we use the 63 sources observed by Swift-XRT at least fifty times (Giommi et al. 2021) as a control sample. Selecting sources with $\nu_{\text{peak}}^S \geq 10^{13.5}$ Hz leaves 34 background objects.

3.2.4 γ -ray band

The FVs for 28 out of 34 G20 sources are available from the 4FGL-DR3 catalogue (Abdollahi et al. 2022). The 4FGL-DR3 catalogue covers 12 years of data in the energy range of 50 MeV-1 TeV and calculates the FVs based on yearly fluxes; in 15 cases $\text{FV} > 0$. As a background sample, we retrieve the FVs for the 4LAC-DR3 blazars with $\nu_{\text{peak}}^S \geq 10^{13.5}$ Hz, for a total of 1628 blazars.

3.3 Flaring state of G20 sources

In addition to their variability, we study the state of the G20 sources at the time of the neutrino arrival. For this, we use the light curves associated with the data described in the previous section. In the optical, however, the ZTF was only commissioned in 2018. Most of the G20 alerts were detected before that date so we additionally use light curves from the All-Sky Automated Survey for Supernovae (ASAS-SN) (Kochanek et al. 2017) provided by de Jaeger et al. (2023) where available. In the γ -ray band, we use the *Fermi*-LAT light curve repository (*Fermi*-LAT LCR) (Abdollahi et al. 2023). The *Fermi*-LAT LCR includes only sources that exceed a minimum threshold of the variability index (21.67), where the variability index is related to the average FV over one year.

4 NEUTRINO DATA FOR MULTI-MESSENGER SEDS

Besides electromagnetic data, we also want to add neutrino information to our SEDs in two complementary ways, namely by estimating fluxes and sensitivities. We then initially use ten years of published

⁸ <https://github.com/mskarl/SINIV-Fermi-SED>

⁹ https://www.swift.ac.uk/swift_portal/

IceCube through-going muon tracks (IceCube Collaboration et al. 2021) to fit, for the first time, each source candidate's neutrino flux. We employ an unbinned maximum likelihood approach (Braun et al. 2008), where we compare a background and a signal hypothesis:

- background hypothesis H_B : the neutrino emission is due to atmospheric background and diffuse astrophysical neutrino emission;
- signal hypothesis H_S : an additional signal component comes from the source and clusters around it. We assume it follows a power law $\propto E^{-\gamma}$. The total neutrino emission observed is the sum of the signal and background components.

This likelihood approach is detailed in Appendix A. In most cases, however, the 68 per cent uncertainties are compatible with no neutrino emission and therefore, we provide only a 68 per cent upper limit (based on Feldman & Cousins 1998).

Furthermore, we show the sensitivity and the discovery potential from Aartsen et al. (2020). The former describes the 90 per cent confidence upper flux limit IceCube can set when there are no events from the source direction. The discovery potential describes the source flux at which IceCube has a 50 per cent chance to make a 5σ discovery (since the number of signal neutrinos produced in a source with a specific flux is Poissonian distributed). For both the sensitivity and the discovery potential, it is assumed the neutrino emission follows a power law with E^{-2} (Aartsen et al. 2020). Since the analysed data set contains only muons, the inferred fluxes are for muon neutrinos and muon antineutrinos. The all-flavour fluxes can be estimated by multiplying the single-flavour flux by a factor of 3.

5 RESULTS

5.1 SEDs

We present the hybrid SEDs in Appendix A. There are 28 cases of the original 49 G20 sources where the best-fit neutrino flux is greater than zero. This applies to 23/34 of the still included sources. However, only in two of these cases, the 68 per cent contours are incompatible with no neutrino flux at all: TXS 0506+056 (4FGL J0509.4+0542) and 3HSP J152835.7+20042 (4FGL J1528.4+2004). In all other cases, we present the upper bound of the 68 per cent uncertainty as a 68 per cent upper flux limit compatible with the best fit. There are three cases where the best-fit spectral index of the neutrino flux is harder than -2 . However, in most cases the number of expected signal neutrinos is quite small, i.e. of the order of one neutrino or less. Thus, the spectra derived with such small numbers of events might change considerably with more data.

5.2 Variability

Variability is one of the properties common to all blazars. Quantifying the amount of this defining property is a fundamental way to investigate the physical mechanisms that power these objects. An estimator that is often used to measure the degree of variability in blazars is the FV parameter (e.g. Schleicher et al. 2019). In the following, we calculate the FV of the G20 sources and of a large control sample in the IR, optical, X-ray, and γ -ray bands.

Following Vaughan et al. (2003) we calculate FV as follows

$$FV = \sqrt{\frac{S^2 - \langle \sigma_{err}^2 \rangle}{\langle f \rangle^2}}, \quad (1)$$

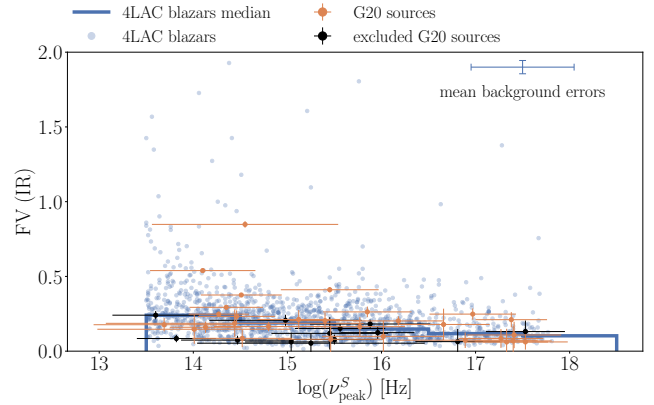


Figure 1. IR FV vs. observed ν_{peak}^S fitted with BlaST. The G20 sources are shown in orange with the respective uncertainties on FV and ν_{peak}^S . We show the excluded G20 sources in black. The background points (in blue) are the 4LAC-DR3 blazars. Average errors for the background sample are depicted in the top right corner. The blue histogram shows the median FV for each decade in ν_{peak}^S . For better readability, the y-axis stops at 2 but there are four background blazars with an FV between 2 and 5.5 not shown (with $13.8 < \log \nu_{peak}^S < 16$).

where S^2 is the variance of the observed fluxes (f) in a given source and σ_{err} is the uncertainty of the single flux measurements.

The statistical error of FV can be calculated as follows

$$\sigma_{FV} = \sqrt{FV^2 + \sqrt{\frac{2 \langle \sigma_{err}^2 \rangle^2}{N \langle f \rangle^4} + \frac{4 \langle \sigma_{err}^2 \rangle FV^2}{N \langle f \rangle^2}}} - FV. \quad (2)$$

We now compare the G20 sources FV in different wavelengths with a background sample of blazars as described in Section 3.2. Table 1 gives all FVs for the G20 sources. A comparison between FVs in different bands would require the same time window and a time binning to properly sample the variability in all bands, which is not our case.

5.2.1 IR band

We have calculated the FV using the $\nu f(\nu)$ flux at $3.4 \mu\text{m}$. The results are reported in Table 1. The FVs of the G20 sources show no significant deviation from the background sample (two-sample Kolmogorov–Smirnov (K-S) test p-value is 0.56). Also, when investigating each decade of ν_{peak}^S , the K-S test does not show significant deviations. There are 14 of 30 source candidates above the median (see Figure 1), which is compatible with the background expectation.

For the background sample, we find the most strongly variable sources with high FVs at lower ν_{peak}^S . The median FV decreases at higher ν_{peak}^S . Hence, in the IR, the median variability shows an anti-correlation with ν_{peak}^S .

5.2.2 Optical band

The optical FVs are reported in Table 1. The FVs of the G20 sources are compatible with those of the background sample (K-S test yields a p-value of 0.91); see Fig. 2. We find 13 out of 29 G20 sources above the background median, which agrees with the background

Table 1. FVs of G20 sources in different bands.

4FGL Name	Name	RA	Dec.	Fractional Variability				$\log(\nu_{\text{peak}}^S)$
(1)	(2)	(3)	(4)	infrared (5)	optical (6)	X-ray (7)	γ -ray (8)	rest-frame [Hz] (9)
4FGL J0158.8+0101	5BZU J0158+0101	01 58 52.776	01 01 32.880	0.18 ± 0.08	0.35 ± 0.06	-	-	13.1 ± 0.5
4FGL J0224.2+1616	VOU J022411+161500	02 24 11.808	16 15 00.000	0.23 ± 0.04	0.38 ± 0.03	-	-	14.7 ± 0.4
<i>4FGL J0232.8+2018</i>	<i>3HSP J023248.5+20171</i>	02 32 48.600	20 17 18.600	0.06 ± 0.05	0.10 ± 0.03	0.28 ± 0.04	-	17.6 ± 0.5
4FGL J0239.5+1326	3HSP J023927.2+13273	02 39 27.216	13 27 38.520	0.2 ± 0.1	0.2 ± 0.1	-	1.4 ± 0.4	14.2 ± 1
4FGL J0244.7+1316	CRATESJ024445+132002	02 44 45.696	13 20 07.080	0.54 ± 0.02	0.16 ± 0.05	-	0.6 ± 0.2	13.3 ± 0.5
<i>4FGL J0344.4+3432</i>	<i>3HSP J034424.9+34301</i>	03 44 24.936	34 30 17.280	0.41 ± 0.02	0.38 ± 0.03	-	-	15.5 ± 0.5
4FGL J0509.4+0542	TXS 0506+056	05 09 25.964	05 41 35.334	0.376 ± 0.007	0.355 ± 0.006	0.64 ± 0.04	0.6 ± 0.1	14.6 ± 0.4
3FGL J0627.9-1517	3HSP J062753.3-15195	06 27 53.376	-15 19 57.000	0.06 ± 0.09	0.16 ± 0.10	-	-	17.4 ± 0.4
4FGL J0649.5-3139	3HSP J064933.6-31392	06 49 33.528	-31 39 20.160	0.25 ± 0.04	-	0.3 ± 0.1	0.6 ± 0.2	17.2 ± 0.5
<i>4FGL J0854.0+2753</i>	<i>3HSP J085410.1+27542</i>	08 54 10.176	27 54 21.600	0.08 ± 0.09	0.1 ± 0.1	-	-	15.7 ± 0.6
<i>4FGL J0946.2+0104</i>	<i>3HSP J094620.2+01045</i>	09 46 20.208	01 04 51.600	0.1 ± 0.1	0.13 ± 0.09	0.2 ± 0.2	0.4 ± 0.2	17.6 ± 0.4
<i>4FGL J0955.1+3551</i>	<i>3HSP J095507.9+35510</i>	09 55 07.882	35 51 00.885	0.11 ± 0.09	0.19 ± 0.05	0.34 ± 0.06	-	17.6 ± 0.5
<i>4FGL J1003.4+0205</i>	<i>3HSP J100326.6+02045</i>	10 03 26.616	02 04 55.560	0.21 ± 0.06	0.20 ± 0.04	0.7 ± 0.2	-	15.3 ± 0.4
4FGL J1055.7-1807	VOU J105603-180929	10 56 03.528	-18 09 30.240	0.85 ± 0.02	0.2 ± 0.1	-	-	15.3 ± 1
4FGL J1117.0+2013	3HSP J111706.2+20140	11 17 06.216	20 14 07.080	0.20 ± 0.03	0.24 ± 0.01	0.42 ± 0.09	0.5 ± 0.1	16.3 ± 0.5
4FGL J1124.0+2045	3HSP J112405.3+20455	11 24 05.352	20 45 52.920	0.20 ± 0.05	0.29 ± 0.03	-	-	15.6 ± 0.4
4FGL J1124.9+2143	3HSP J112503.6+21430	11 25 03.552	21 43 04.080	0.16 ± 0.06	0.19 ± 0.08	-	-	16.0 ± 0.5
<i>3FGL J1258.4+2123</i>	<i>3HSP J125821.5+21235</i>	12 58 21.456	21 23 51.000	0.1 ± 0.1	0.0 ± 0.2	-	-	16.2 ± 0.7
4FGL J1258.7-0452	3HSP J125848.0-04474	12 58 48.048	-04 47 45.240	0.21 ± 0.05	0.23 ± 0.03	0.38 ± 0.07	0.8 ± 0.3	17.6 ± 0.4
4FGL J1300.0+1753	3HSP J130008.5+17553	13 00 08.520	17 55 37.560	0.19 ± 0.09	0.20 ± 0.07	-	0.1 ± 0.6	14.2 ± 1
4FGL J1314.7+2348	5BZB J1314+2348	13 14 43.800	23 48 26.640	0.539 ± 0.007	0.28 ± 0.01	-	0.23 ± 0.07	14.3 ± 0.6
4FGL J1321.9+3219	5BZB J1322+3216	13 22 47.400	32 16 08.760	0.18 ± 0.04	0.27 ± 0.02	-	0.8 ± 0.3	14.0 ± 0.8
4FGL J1507.3-3710	VOU J150720-370902	15 07 20.808	-37 09 02.880	0.25 ± 0.02	-	-	-	14.4 ± 0.3
4FGL J1528.4+2004	3HSP J152835.7+20042	15 28 35.784	20 04 20.280	0.2 ± 0.1	0.28 ± 0.06	0.6 ± 0.2	-	16.9 ± 0.5
<i>4FGL J1533.2+1855</i>	<i>3HSP J153311.2+18542</i>	15 33 11.256	18 54 29.160	0.08 ± 0.06	0.11 ± 0.08	0.1 ± 0.2	-	17.4 ± 0.5
<i>4FGL J1554.2+2008</i>	<i>3HSP J155424.1+20112</i>	15 54 24.120	20 11 25.080	0.07 ± 0.05	0.10 ± 0.04	0.40 ± 0.09	-	17.0 ± 0.8
4FGL J1808.2+3500	CRATESJ180812+350104	18 08 11.544	35 01 18.840	0.29 ± 0.01	0.426 ± 0.004	-	0.5 ± 0.1	14.4 ± 0.4
4FGL J1808.8+3522	3HSP J180849.7+35204	18 08 49.704	35 20 43.080	0.16 ± 0.03	0.29 ± 0.03	-	-	14.9 ± 0.6
<i>4FGL J2030.5+2235</i>	<i>3HSP J203031.6+22343</i>	20 30 31.096	22 34 37.019	0.08 ± 0.04	0.25 ± 0.06	-	-	16.2 ± 0.4
4FGL J2030.9+1935	3HSP J203057.1+19361	20 30 57.120	19 36 12.960	0.26 ± 0.04	0.15 ± 0.02	-	0.3 ± 0.1	15.9 ± 0.5
<i>4FGL J2133.1+2529</i>	<i>3HSP J213314.3+25285</i>	21 33 14.352	25 28 59.160	0.09 ± 0.06	0.16 ± 0.05	-	-	14.6 ± 0.5
<i>4FGL J2223.3+0102</i>	<i>3HSP J222329.5+01022</i>	22 23 29.520	01 02 26.160	-	0.31 ± 0.03	-	0.4 ± 0.6	14.9 ± 0.4
4FGL J2227.9+0036	5BZB J2227+0037	22 27 58.152	00 37 05.520	0.16 ± 0.04	0.19 ± 0.03	-	0.3 ± 0.1	14.4 ± 0.4
4FGL J2326.2+0113	CRATESJ232625+011147	23 26 25.632	01 12 08.640	0.82 ± 0.01	1.071 ± 0.006	-	1.0 ± 0.3	13.8 ± 0.5
4FGL J0103.5+1526	3HSP J010326.0+15262	01 03 26.016	15 26 24.720	0.05 ± 0.06	0.14 ± 0.05	-	-	15.1 ± 1
<i>4FGL J0339.2-1736</i>	<i>3HSP J033913.7-17360</i>	03 39 13.703	-17 36 00.783	0.08 ± 0.03	0.19 ± 0.01	0.1 ± 0.3	0.2 ± 0.1	15.5 ± 0.5
4FGL J0525.6-2008	CRATESJ052526-201054	05 25 28.032	-20 10 48.360	-	0.18 ± 0.02	-	0.3 ± 0.3	13.4 ± 0.5
4FGL J1040.5+0617	GB6 J1040+0617	10 40 31.632	06 17 21.840	0.698 ± 0.008	1.011 ± 0.008	0.5 ± 0.3	0.9 ± 0.2	13.7 ± 0.5
4FGL J1043.6+0654	5BZB J1043+0653	10 43 23.880	06 53 09.960	0.1 ± 0.1	0.2 ± 0.1	-	-	15.6 ± 0.6
<i>4FGL J1230.8+1223</i>	<i>M87</i>	12 30 49.440	12 23 30.120	0.08 ± 0.02	0.340 ± 0.004	0.24 ± 0.03	0.14 ± 0.06	13.8 ± 0.4
<i>4FGL J1231.5+1421</i>	<i>3HSP J123123.1+14212</i>	12 31 23.928	14 21 24.120	0.15 ± 0.03	0.20 ± 0.05	-	0.3 ± 0.2	15.7 ± 0.5
<i>4FGL J1359.1-1152</i>	<i>VOU J135921-115043</i>	13 59 21.312	-11 50 43.800	0.06 ± 0.08	-	0.3 ± 0.5	-	16.9 ± 0.5
4FGL J1404.8+6554	3HSP J140449.6+65543	14 04 49.632	65 54 30.960	0.18 ± 0.03	0.18 ± 0.02	0.5 ± 0.1	0.5 ± 0.1	16.0 ± 0.6
4FGL J1439.5-2525	VOU J143934-252458	14 39 34.656	-25 24 58.320	0.06 ± 0.06	0.14 ± 0.06	-	-	15.1 ± 0.5
4FGL J1440.0-2343	3HSP J143959.4-23414	14 39 59.424	-23 41 40.200	0.21 ± 0.04	0.18 ± 0.05	-	0.3 ± 0.2	15.1 ± 0.8
4FGL J1447.0-2657	3HSP J144656.8-26565	14 46 56.832	-26 56 58.200	0.13 ± 0.07	0.15 ± 0.09	0.2 ± 0.2	-	17.6 ± 0.4
4FGL J2350.6-3005	3HSP J235034.3-30060	23 50 34.368	-30 06 03.240	0.12 ± 0.04	-	-	0.5 ± 0.1	16.1 ± 0.4
4FGL J2351.4-2818	IC 5362	23 51 36.672	-28 21 53.280	0.07 ± 0.03	-	-	-	14.5 ± 0.6
4FGL J2358.1-2853	CRATESJ235815-285341	23 58 16.968	-28 53 34.080	0.24 ± 0.03	-	-	-	14.0 ± 0.5

Notes. FVs of G20 sources for different wavelengths (columns 5 to 8). The γ -ray FVs are taken from the 4FGL-DR3 catalogue and only listed here if $\text{FV} > 0$. ν_{peak}^S is given in the last column as estimated with BlaST in the rest-frame, corrected for the redshift. The first section lists the 34 G20 sources that remain after removing excluded sources. Masquerading sources are listed in bold font, sources where the extension of the best-fit γ -ray flux meets the neutrino best-fit or the 5σ discovery potential line are listed in italics (see Section 6 and SEDs in Appendix A). The bottom section lists sources excluded because of the revised alert criteria (see Section 2).

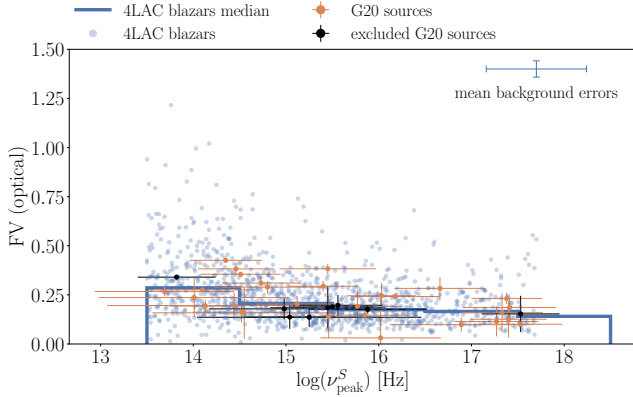


Figure 2. Optical FV vs. observed ν_{peak}^S fitted with BlaST. The G20 sources are shown in orange with the respective uncertainties for FV and ν_{peak}^S . We show the excluded G20 sources in black. The background points (in blue) are the 4LAC-DR3 blazars with optical data from the ZTF (blue dots). Average errors for the background sample are depicted in the top right corner. The blue histogram shows the median FV for each decade in ν_{peak}^S . For better readability, the y-axis stops at 1.5 but there is one background blazar with $FV = 3.3$ and $\log \nu_{\text{peak}}^S \sim 14$.

expectation. We observe the same trend as in the IR, with the median FV decreasing for higher ν_{peak}^S .

5.2.3 X-ray band

The FV X-ray results are reported in Table 1. Notice that, as in the γ -ray case, the errors here are larger than in the optical/IR bands, where the individual uncertainties are smaller and the number of data points is higher. For the X-ray light curves, the FV varies for different SWIFT snapshots, which indicates short-term variability for the G20 sources. Here, we take the flux of the total observation for the FV calculation (see Fig. 3). A two-sample K-S test comparing the background sample with the G20 sources yields a p-value of 0.025. We find significantly less variability in the G20 sources compared to the background sample (10 out of 11 sources are below the median background FV). This difference is likely to be the result of a selection bias in the background sample for highly variable sources, as less variable sources might have been of less interest for repeated Swift-XRT observations.

5.2.4 γ -ray band

In the γ -ray band we compare the variability fraction of the G20 sources with that of the background sample (Table 1 and Fig. 4). For this, we take all events within one decade of ν_{peak}^S and run a two-sample K-S test comparing background and G20 sources. In total, we get a p-value of 0.19.

We also compare the fraction of objects that have no reported FV. For the background sample, 66 per cent of objects have $FV = 0$. For the G20 objects, there are 46 per cent of objects without a reported FV. This is compatible with the background assumption (p-value of 0.04).

When considering only objects with $FV > 0$, we test if there is a significant number of G20 sources above the background sample's median FV for each ν_{peak}^S band (see Fig. 4). We find 9 out of 13 G20 sources above the background median FV, corresponding to a

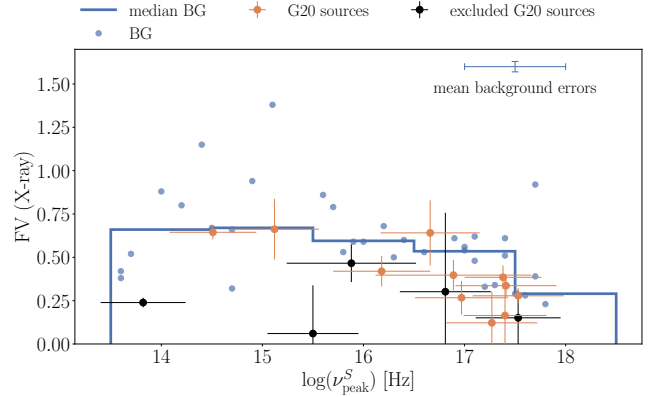


Figure 3. FV in X-rays vs. observed ν_{peak}^S fitted with BlaST. The G20 sources are shown in orange with the respective uncertainties for FV and ν_{peak}^S . We show the excluded G20 sources in black. The background points (in blue) are from the sample of sources observed at least 50 times with SWIFT (Giommi et al. 2021). Average errors for the background sample are depicted in the top right corner. The blue histogram shows the median FV for each decade in ν_{peak}^S .

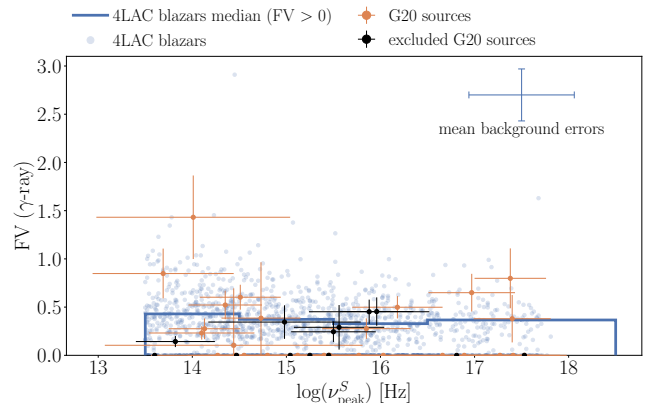


Figure 4. The FV, as given in the 4FGL catalogue, vs. observed ν_{peak}^S as estimated with BlaST. The orange dots with error bars show the 4FGL FV for the G20 sources. We show the excluded G20 sources in black. The background sample (blue) are all blazars in the 4LAC catalogue. Average errors for the background sample are depicted in the top right corner. The blue histogram shows the median FV for each decade in ν_{peak}^S for the background sources with $FV > 0$.

p-value of 0.13. Hence, we do not find any difference between the background sample and the G20 sources for the γ -ray FV.

5.3 State of G20 sources during neutrino arrival times

The high-energy neutrino IceCube-170922A was detected while TXS 0506+056 was flaring (IceCube Collaboration et al. 2018b,a). To search for similar patterns with all the G20 alert events and G20 sources we investigate the state of the source candidate with the light curves used in the variability study. We define flares in a similar fashion to de Jaeger et al. (2023). For each light curve, we determine flux bins with Bayesian blocks (Scargle 1998; Scargle et al. 2013). We use the same parameters for each source, assuming point measures (as in Scargle et al. 2013, Section 3.3 with the default

value of $p_0 = 0.05$ in equation 21 of Scargle et al. 2013) with the flux uncertainties as σ . We define a flare where the flux in a bin, F_{bin} , exceeds the average flux plus the standard deviation over the whole light curve. We calculate the chance probability, P_{BG} , as the fraction of flaring time vs. the total data taking time. Finally, we do a binomial test for the total number of neutrinos observed coincident with a flaring source based on the chance probability for all sources combined. The following analysis excludes the objects in the bottom section of Table 1. We list all results for each source in all bands in the appendix in Table A2 and show example light curves for TXS 0506+056 in Figure A1.

5.3.1 IR band

In the IR band we examine the NEOWISE light curves as described in Section 3.2. Out of 33 light curves, we find three sources where the neutrino arrival coincides with a flare per the above definition (TXS 0506+056 [4FGL J0509.4+0542], 3HSP J064933.6-31392 [4FGL J0649.5-3139], and 3HSP J125848.0-04474 [4FGL J1258.7-0452]). The chance probability is 0.131. The binomial probability p_{binom} , of finding three sources out of 33 given this chance probability is compatible with the background assumption ($p_{\text{binom}} = 0.79$).

5.3.2 Optical band

In total, there are nine optical light curves (with three light curves from ZTF and six light curves from ASAS-SN) during the respective neutrino arrival time. Out of these nine, we find two sources where the neutrino is coincident with a flare (TXS 0506+056 [4FGL J0509.4+054] and 3HSP J100326.6+02045 [4FGL J1003.4+0205]). The chance probability is 0.112. Another binomial test of getting two sources out of nine given this chance probability yields a p-value compatible with background ($p_{\text{binom}} = 0.27$).

5.3.3 X-ray band

In X-rays, nine out of 25 sources with X-ray data have sufficiently sampled light curves to allow flare identification. Two sources are identified where the neutrino arrival is coincident with an X-ray flare (3HSP J023248.5+201717 [4FGL J0232.8+2018] and 3HSP J095507.9+355101 [4FGL J0955.1+3551]). For all sources combined, the chance probability is 0.097. A binomial test of getting two sources based on this chance probability yields a p-value compatible with background ($p_{\text{binom}} = 0.22$).

5.3.4 γ -ray band

We find eight light curves for the G20 sources in the *Fermi*-LAT LCR database. Out of these eight, there is one case where the neutrino arrives simultaneously with a γ -ray flare: TXS 0506+056. The chance probability for finding a coincidence is 0.006. The binomial probability of finding one source out of eight based on this chance probability is 0.045 or 1.7σ .

Table 2 summarises the results for each wavelength, listing the number of available light curves, the chance probabilities, and the result of the binomial test for finding neutrinos arriving coincident with a flaring source. Only in γ -rays we find a non-background binomial p-value of 1.7σ , due to the neutrino IceCube-170922A arriving during a flaring period of TXS 0506+056.

Table 2. Results of the search for neutrino alerts arriving coincident with flares in different bands.

Wavelength	N_{LC}	P_{BG}	N_{coinc}	p_{binom}
IR	33	0.131	3	0.79
Optical	9	0.112	2	0.27
X-ray	9	0.097	2	0.22
γ -ray	8	0.006	1	0.045

Notes. We list the number of available light curves, N_{LC} , suitable to identify flares, the chance probability, P_{BG} , of a neutrino arriving during a flare, the number of coincidences, N_{coinc} , found in these light curves and the p-value of the binomial test, p_{binom} , for finding N_{coinc} given P_{BG} .

6 DISCUSSION

6.1 Hybrid SEDs

For the first time we have a sizeable number of blazars, 34 per cent of which might be neutrino sources, with an estimate of their neutrino fluxes. Based on purely hadronic models we would expect $E_\gamma \approx 2 \times E_\nu$ and $F_\gamma \approx 2 \times F_\nu$ (e.g. Kelner & Aharonian 2008). Therefore, we can have three extreme cases: (1) $F_\gamma \approx F_\nu$, which implies that in both bands the emission is hadronic; (2) $F_\gamma \ll F_\nu$, which would suggest that γ -ray emission is absorbed and high-energy emission is degraded to lower energies through cascades; (3) $F_\gamma \gg F_\nu$, which would suggest that γ -ray emission is mainly leptonic. However, all the above assumes that the sampled γ -ray and neutrino energies are similar, which is not the case, as while all sources have F_γ in the 0.1 – 100 GeV range, the neutrino energies used to derive the best fit flux are higher and vary from source to source (see Fig. A2 and Appendix A).

We then took the alternative but relatively robust approach of looking at the hybrid SEDs to see if the extension of the best-fit γ -ray flux met the neutrino best-fit or the 5σ discovery potential line (somewhat similarly to what was done by Padovani & Resconi 2014). It turned out that in 18 out of 34 cases this was the case (those objects are highlighted in italic in Table 1 and in the SEDs in Appendix A). As a first approximation, we take the 15 excluded sources as a (very small) background sample. In that case we find 5 out of 15 sources fulfilling the same requirement, yielding a background probability of 0.33. A binomial test calculating the chance of getting 18 out of 34 objects with such a probability is incompatible with the background assumption only at the 2.2σ level.

As an alternative approach, we check where the best-fit neutrino flux exceeds 0. In the background sample, we find 3 objects with a best-fit neutrino flux > 0 . This yields a background probability of 0.2. Comparing this with the investigated sources we find 27 objects with a best-fit neutrino flux > 0 . A binomial test of getting 27 objects out of 34 with a background probability of 0.2 yields a highly significant p-value above the 5σ level. This result, however, depends strongly on the statistics and changes significantly when adding/removing a few sources from the signal/background sample. Furthermore, in 11 of the 27 cases with a best-fit neutrino flux > 0 , the lower 68 per cent uncertainty of the neutrino flux is compatible with a flux of 0 (and in 16 cases it is incompatible with a flux of 0 at the 68 per cent confidence level). As a further test, we can compare this with the background sample where we fit a flux incompatible with 0 at the 68 per cent level for 2 sources out of 15, and the binomial test results in 4.6σ . We emphasize that this result is based on a small background sample of 15 sources. Hence, we

exercise caution concerning the reliability of these tests because of the small background sample size.

Paper III did not find any significant difference between the G20 sources and a control sample of IHLs in terms of their radio and γ -ray powers, and ν_{peak}^S , although it was stated that the lack of such differences could have been due to the relatively small number of G20 sources, in which only less than half of the sources were expected to be associated with astrophysical neutrinos. A redshift difference was found but was explained in terms of a selection effect. In this work, we investigate the flux at ν_{peak}^S , as an approximation of the source's bolometric flux and hence a measure of the blazar's total power, as neutrino emission might be related to the total emitted radiation. We find no differences between the fluxes at ν_{peak}^S between the G20 sources and the blazars in the 4LAC-DR3 catalogue (p-value of two-sample K-S test is 0.73).

In Paper III, masquerading BL Lacs turned out to be more powerful than the non-masquerading ones in the radio and γ -ray band, with a smaller ν_{peak}^S . This is to be expected, as these are the properties, which allow them to dilute their strong, FSRQ-like emission lines effectively. When comparing the flux at ν_{peak}^S of masquerading sources with non-masquerading sources in our sample, we find no difference between the two classes (with a p-value of 0.14 for a two-sample K-S test).

6.2 Variability

We find no significant difference in variability in the IR, optical, and γ -ray bands for the G20 sources compared to the 4LAC-DR3 background sample or the 63 sources in [Giommi et al. \(2021\)](#) for the X-ray band. Moreover, when comparing masquerading BL Lacs with non-masquerading BL Lacs, we also find no significant differences in FVs (the best two-sample K-S test p-value was 0.048 in the X-ray band).

However, several caveats should be considered. For example, light curves for the majority of the G20 sources are only available in the IR and optical bands. In the X-rays, only a limited number of observations are available with sufficient flux measurements for generating light curves. In some cases, we find rapid short-term variability within one observing period. However, the number of measurements where detecting such short-term variability is possible is limited in our sample. Hence, we take the average flux levels for one observation to generate the light curve. In the X-ray background sample, we are limited by the lack of observations for a broad population of blazars.

In the γ -rays we used the available FVs in the 4FGL-DR3 catalogue, which are calculated based on yearly fluxes. Hence, we have differently binned light curves for different bands, which hinders the comparison of FVs between different bands. A custom generation of *Fermi*-LAT light curves and calculation of FVs would be needed.

In general, the results of the different bands cannot be compared with each other since that would require similar binning and data coverage. Some light curves are only sparsely sampled (for example in the X-ray band as listed in Table A1). Additionally, also within one band, the light curves are not uniformly sampled and vary greatly in sampling frequency (see again Table A1), which can impact the individual FV comparison. However, since we look at the FV distribution of many objects and compare them with a large background population, we expect the impact to be averaged out.

6.3 Flares

We do not find a significant correlation of flares in the IR, optical, X-ray or γ -ray bands, and the arrival times of high-energy neutrinos. This agrees with the results of [Chang et al. \(2022\)](#), who studied the temporal correlations of blazar flares in the millimetre, IR, X-ray, and γ -ray bands with IceCube neutrino alerts, with no significant results. Also [Hovatta et al. \(2021\)](#) did not find a significant correlation between strongly radio flaring blazars and IceCube events.

In this work, TXS 0506+056 is the only source where flares in the IR, optical, and γ -rays coincide with the neutrino arrival; in the X-rays there is no flare at 1 keV, only when looking at larger energies the source shows flaring behaviour ([IceCube Collaboration et al. 2018b](#)). All other cases are restricted to one wavelength only. However, there were very few cases when relevant data were available directly at the neutrino arrival time; hence the state of most G20 sources at the time of neutrino arrival is simply not known. This emphasises the importance of immediate multi-wavelength follow-up observations of IceCube alert events.

7 CONCLUSIONS AND SUMMARY

We have presented the multi-wavelength and neutrino SEDs for a selection of potential neutrino sources based on [Giommi et al. \(2020\)](#). The selection was updated by excluding objects not matching the revised criteria of [Abbasi et al. \(2023\)](#). For the SEDs, we obtained the low-energy multi-frequency data with VOU-Blazars. We included γ -ray data from the *Fermi*-LAT telescope and a best-fit of the γ -ray SEDs. Additionally, we analysed 10 years of publicly available neutrino data from the IceCube Neutrino Observatory. We derived for the first time the best-fit neutrino fluxes (assuming a power-law spectrum) in 27 cases where the best-fit flux is greater than 0. The 68 per cent confidence levels are compatible with no flux in 11 out of 27 cases. We included the IceCube 5σ discovery potential and sensitivity in the SEDs based on [Aartsen et al. \(2020\)](#).

Looking for signatures of hadronic production, we took the extension of the best-fit γ -ray flux and checked if it met the neutrino best-fit or the 5σ discovery potential. Comparing the updated selection with the excluded objects yielded a 2.2σ association of sources with matching γ -ray and neutrino fluxes in our sample. Otherwise, comparing the number of sources where we fit fluxes incompatible with 0 at the 68 per cent confidence level, we find a 4.6σ over fluctuation for our source selection. However, we emphasize that this result is based on a small background selection of 15 sources and requires confirmation with better statistics.

As a next step, we used the obtained data to study the sources' variability in the IR, optical, γ -ray, and X-ray bands. For the first three bands we used the blazars of the 4LAC-DR3 catalogue as a background sample. For the latter, we used a selection of 63 blazars observed with Swift-XRT at least fifty times ([Giommi et al. 2021](#)). We found no significant differences in the variability of our sources compared with the background samples.

Furthermore, we checked for coincidences of the high-energy neutrino arrival time and flaring states of the source candidates, finding no significant correlation in any of the bands. However, in most cases there were no observations available at the time of neutrino arrival, which emphasises the importance of fast follow-up observations of the astronomical community.

Finally, we found no significant differences in the SEDs of the G20 sources compared with selections of a general population of blazars. We compared the flux at ν_{peak}^S as a measure of the blazar's

total emission. The G20 sources show no differences in their flux distributions compared to blazars of the 4LAC-DR3 catalogue. Both results, however, could be related to the relatively small number of G20 sources. Furthermore, when comparing masquerading with non-masquerading sources, we also find no differences in their flux distributions at ν_{peak}^S .

The next step for the SIN project will be the modelling of the hybrid SEDs put together in this paper with a lepto-hadronic code to assess the physical likelihood of a connection between blazars and neutrinos (Rodrigues et al., in preparation).

ACKNOWLEDGMENTS

We thank Maria Petropoulou and Xavier Rodrigues for helpful discussions and the referee for her/his useful comments and suggestions. We acknowledge the use of data and software facilities from the SSDC, managed by the Italian Space Agency, and the United Nations “Open Universe” initiative. This work is supported by the Deutsche Forschungsgemeinschaft through grant SFB 1258 “Neutrinos and Dark Matter in Astro- and Particle Physics”.

DATA AVAILABILITY

Most of the data used in this paper are publicly available from the VOU-Blazars package, from the Firmamento online tool at <https://firmamento.hosting.nyu.edu>, and from the Zwicky Transient Facility web pages at <https://www.ztf.caltech.edu/>. Specific data can be provided by the lead author upon reasonable request.

REFERENCES

- Aartsen M. G., et al., 2020, *Phys. Rev. Lett.*, **124**, 051103
 Abbasi R., et al., 2022a, *arXiv e-prints*, p. [arXiv:2210.04930](https://arxiv.org/abs/2210.04930)
 Abbasi R., et al., 2022b, *Science*, **378**, 538
 Abbasi R., et al., 2023, IceCat-1: the IceCube Event Catalog of Alert Tracks ([arXiv:2304.01174](https://arxiv.org/abs/2304.01174))
 Abdo A. A., et al., 2010, *ApJ*, **716**, 30
 Abdollahi S., et al., 2022, *ApJS*
 Abdollahi S., et al., 2023, *ApJS*, **265**, 31
 Ackermann M., et al., 2012, *The Astrophysical Journal Supplement Series*, **203**, 4
 Ajello M., et al., 2020, *The Astrophysical Journal*, **892**, 105
 Bellenghi C., et al., 2023, in Proceedings of 38th International Cosmic Ray Conference — PoS(ICRC2023). p. 1061, [doi:10.22323/1.444.1061](https://doi.org/10.22323/1.444.1061)
 Bellm E. C., et al., 2019, *PASP*, **131**, 018002
 Blaufuss E., Kintscher T., Lu L., Tung C. F., 2019, The Next Generation of IceCube Realtime Neutrino Alerts ([arXiv:1908.04884](https://arxiv.org/abs/1908.04884))
 Braun J., Dumm J., De Palma F., Finley C., Karle A., Montaruli T., 2008, *Astrophys. J.*, **29**, 299
 Chang Y.-L., Brandt C. H., Giommi P., 2020, *Astronomy and Computing*, **30**, 100350
 Chang Y.-L., Arsioli B., Li W., Xu D., Chen L., 2022, *ApJ*, **939**, 123
 Costamante L., Bonoli G., Tavecchio F., Ghisellini G., Tagliaferri G., Khangulyan D., 2018, *Monthly Notices of the Royal Astronomical Society*, **477**, 4257
 Feldman G. J., Cousins R. D., 1998, *Physical Review D*, **57**, 3873
 Giommi P., Padovani P., 2021, *Universe*, **7**, 492
 Giommi P., Glauch T., Padovani P., Resconi E., Turcati A., Chang Y. L., 2020, *MNRAS*, **497**, 865
 Giommi P., et al., 2021, *MNRAS*, **507**, 5690
 Glauch T., Kerscher T., Giommi P., 2022, *Astronomy and Computing*, **41**, 100646

- Hovatta T., et al., 2021, *A&A*, **650**, A83
 IceCube Collaboration 2013, *Science*, **342**, 1242856
 IceCube Collaboration et al., 2018a, *Science*, **361**, 147
 IceCube Collaboration et al., 2018b, *Science*, **361**, eaat1378
 IceCube Collaboration et al., 2021, *arXiv e-prints*, p. [arXiv:2101.09836](https://arxiv.org/abs/2101.09836)
 Kelner S. R., Aharonian F. A., 2008, *Phys. Rev. D*, **78**, 034013
 Kochanek C. S., et al., 2017, *PASP*, **129**, 104502
 Lott B., Gasparrini D., Ciprini S., 2020, *arXiv e-prints*, p. [arXiv:2010.08406](https://arxiv.org/abs/2010.08406)
 Mainzer A., et al., 2014, *ApJ*, **792**, 30
 Padovani P., Giommi P., 1995, *ApJ*, **444**, 567
 Padovani P., Resconi E., 2014, *MNRAS*, **443**, 474
 Padovani P., et al., 2017, *A&ARv*, **25**, 2
 Padovani P., Oikonomou F., Petropoulou M., Giommi P., Resconi E., 2019, *MNRAS*, **484**, L104
 Padovani P., et al., 2022, *MNRAS*, **510**, 2671
 Paiano S., Falomo R., Treves A., Padovani P., Giommi P., Scarpa R., 2021, *MNRAS*, **504**, 3338
 Paiano S., Falomo R., Treves A., Padovani P., Giommi P., Scarpa R., Bisogni S., Marini E., 2023, *MNRAS*, **521**, 2270
 Petropoulou M., Dimitrakoudis S., Padovani P., Mastichiadis A., Resconi E., 2015, *MNRAS*, **448**, 2412
 Petropoulou M., Oikonomou F., Mastichiadis A., Murase K., Padovani P., Vasilopoulos G., Giommi P., 2020, *ApJ*, **899**, 113
 Scargle J. D., 1998, *ApJ*, **504**, 405
 Scargle J. D., Norris J. P., Jackson B., Chiang J., 2013, *ApJ*, **764**, 167
 Schleicher B., et al., 2019, *Galaxies*, **7**, 62
 Vaughan S., Edelson R., Warwick R. S., Uttley P., 2003, *MNRAS*, **345**, 1271
 Wood M., Caputo R., Charles E., Di Mauro M., Magill J., Perkins J. S., Fermi-LAT Collaboration 2017, in 35th International Cosmic Ray Conference (ICRC2017). p. 824 ([arXiv:1707.09551](https://arxiv.org/abs/1707.09551)), [doi:10.22323/1.301.0824](https://doi.org/10.22323/1.301.0824)
 Wright E. L., et al., 2010, *AJ*, **140**, 1868
 de Jaeger T., et al., 2023, *MNRAS*, **519**, 6349

APPENDIX A:

VOU-BLAZARS CATALOGUES

The catalogues queried in VOU-Blazars are: NVSS, FIRST, SUMSS, VLASSQL, 2SXPS, SDS82, 1OUSX, RASS, XMMSL2, 4XMM-DR11, BMW, WGACAT, IPC2E, IPCSL, Chandra-CSC2, MAXI, eROSITA-EDR, ZWCLUSTERS, PSZ2, ABELL, MCXC, 5BZCat, SDSSWHL, SWXCS, 3HSP, FermiGRB, MilliQuas, BROs, MST9Y, PULSAR, F2PSR, F357cat, XRTDEEP, WISH352, GLEAM, TGSS150, VLSSR, LoTSS, PMN, GB6, GB87, ATPMN, AT20G, NORTH20, CRATES, F357det, KUEHR, PCNT, PCCS44, PCCS70, PCCS100, PCCS143, PCCS217, PCCS353, PCCS2, ALMA, SPIRE, H-ATLAS-DR1, H-ATLAS-DR2, H-ATLAS-DR2NGP, H-ATLAS-DR2SGP, AKARIBSC, IRAS-PSC, WISE, WISEME, NEOWISE, 2MASS, USNO, SDSS, HSTGSC, PanSTARRS, GAIA, SMARTS, UVOT, GALEX, XMMOM, CMA, EXOSAT, XRTSPEC, OUSXB, OUSXG, OULC, BAT105m, BEP-POSAX, NuBlazar, 3FHL, 2FHL, 3FGL, 2BIGB, 4FGL-DR3, 2AGILE, FermiMeV, FMonLC.

NEUTRINO FLUXES

As mentioned in Section 4, we use an unbinned maximum likelihood approach (Braun et al. 2008), to compare a signal, H_S , and a background hypothesis, H_B .

We take the ratios of these likelihoods and optimise the signal likelihood by varying the source flux, Φ , which is described by the number of observed signal neutrinos, n_S , and their energy distribution. Neutrinos are produced via particle interaction in a

source, and the number of produced neutrinos is thus Poissonian distributed. The fitted number of signal neutrinos, n_S , is hence the mean number of neutrinos we expect to see in the detector for a respective flux. We fit the energy spectral index, γ , for the energy distribution. The optimised expression is (Braun et al. 2008):

$$\text{TS} = -2 \ln \frac{\sup \mathcal{L}(H_B)}{\sup \mathcal{L}(H_S)} = 2 \sum_i \ln \left[\frac{n_S}{N} \left(\frac{S_i}{B_i} - 1 \right) + 1 \right], \quad (\text{A1})$$

with N as the total number of observed events and a signal, S_i , and background, B_i , probability density function (pdf) for each event i . The signal pdf includes a spatial clustering around the source position \vec{x}_S and the probability of detecting a neutrino with reconstructed energy, E_i , originating from declination, δ_i , for a source emitting neutrinos with a spectrum $E^{-\gamma}$. The latter part is extracted from the effective area and the smearing matrix in the data release. We use the reconstructed event properties, i.e., origin direction, $\vec{x}_i = (\alpha_i, \delta_i)$, the uncertainty on the directional reconstruction, σ_i , and the reconstructed muon energy, E_i , to define the signal pdf (Braun et al. 2008)

$$\begin{aligned} S_i &= S_{\text{spatial}}(\vec{x}_i, \sigma_i | \vec{x}_S) \cdot S_{\text{energy}}(E_i | \delta_i, \gamma) \\ &= \frac{1}{2\pi\sigma_i^2} \exp\left(-\frac{|\vec{x}_i - \vec{x}_S|^2}{2\sigma_i^2}\right) \cdot S_{\text{energy}}(E_i | \delta_i, \gamma). \end{aligned} \quad (\text{A2})$$

The background pdfs, B_i , are (Braun et al. 2008)

$$B_i = B_{\text{spatial}}(\vec{x}_i) \cdot B_{\text{energy}}(E_i | \delta_i) = \frac{1}{2\pi} \cdot P(\delta_i) \cdot B_{\text{energy}}(E_i | \delta_i). \quad (\text{A3})$$

Here, the spatial term is uniform in right ascension, α_i , for the background for integration times greater than a day since IceCube is located at the South Pole. The energy term describing the probability of detecting an event with energy E_i at declination δ_i is extracted from the effective area and the smearing matrix published in the data release. With the detector's effective area and the smearing matrix, we calculate the neutrino flux corresponding to n_S .

We then use the approach in Feldman & Cousins (1998) to estimate confidence intervals. We repeatedly simulate neutrino emission of various strengths for each source, following a power-law energy distribution of $\propto E^{-\gamma}$, with $\gamma \in [1, 3.7]$. We stop at 3.7 since such soft spectral indices simulate a neutrino flux similar to the atmospheric background. With equation A1, we get a distribution of TS values for each simulated flux. Based on this TS distribution, we determine the 68 per cent confidence belt. In most cases, the lower limit is compatible with no neutrino emission from the source, and we show the upper level as 68 per cent upper limit. The parameter optimisation and the flux simulations are done with the open-source framework SkyLLH¹⁰ (Bellenghi et al. 2023).

The data provides the reconstructed properties, θ_r , i.e. reconstructed origin in declination, δ_i , the reconstructed energy, E_i , and the reconstructed spatial uncertainty, σ_i . However, we want to know for which true neutrino energies, E_{true} , our flux estimation is valid. With the data given in the public data release, we construct the probability to observe the true energy given the reconstructed parameter:

$$P(E_{\text{true}} | \theta_r) = \frac{P(\theta_r | E_{\text{true}})P(E_{\text{true}})}{P(\theta_r)}, \quad (\text{A4})$$

always for a given flux Φ at a given declination δ_i . We get $P(\theta_r | E_{\text{true}})$ from the smearing matrix in the data release as the fractional counts ($N_{\text{reco}, E_{\text{true}}} / N_{E_{\text{true}}}$). The probability for the true energy, $P(E_{\text{true}})$, can be calculated with the effective area. The effective area, A_{eff} , yields the number of expected events, N_{obs} , for a given flux, Φ , in the energy range E_0 to E_1 and during detection time T :

$$N_{\text{obs}} = \int_{E_0}^{E_1} \int_{t_0}^T \Phi(E) A_{\text{eff}}(E) dE dt. \quad (\text{A5})$$

The probability to get an event with true Energy, E_{true} , is $P(E_{\text{true}}) = N_{E_{\text{true}}} / N_{\text{all}}$. We assume E_{true} lies within the energy bin with edges E_0 and E_1 of the effective area matrix:

$$P(E_{\text{true}}) = \frac{N_{E_{\text{true}}}}{N_{\text{all}}} = \frac{\int_{E_0}^{E_1} \int_{t_0}^T \Phi(E) A_{\text{eff}}(E) dE dt}{\int_{E_{\text{min}}}^{E_{\text{max}}} \int_{t_0}^T \Phi(E) A_{\text{eff}}(E) dE dt}, \quad (\text{A6})$$

where the time integral is given by the total uptime of the detector in each respective data sample. $P(\theta_r) = \sum_{E_{\text{true}}} P(\theta_r | E_{\text{true}}) P(E_{\text{true}})$ and can be calculated with the above quantities.

With this, we can get $P(E_{\text{true}} | \theta_r)$ for each sample. The IceCube public data is published as distinct data samples with each their own effective area distribution and smearing (describing the reconstruction in the detector).

Suppose we want one combined probability over all samples. In that case, we weigh each contribution with the ratio of the sample effective area over the summed effective area of all samples (for a respective declination and true energy). We then scale each sample contribution with this factor:

$$\text{sample contribution} = \frac{\int_{E_0}^{E_1} A_{\text{eff, sample}}(E) dE}{\sum_{\text{samples}} \int_{E_0}^{E_1} A_{\text{eff, sample}}(E) dE}. \quad (\text{A7})$$

Hence, each bin entry is $P(E_{\text{true}} | \theta_r) \times \text{sample contribution}$, and we can take the sum over all samples for each bin to get the true energy distribution. We evaluate the true energy distribution for all n_S events that contribute most to the flux (i.e., those events where the signal pdf divided by the background pdf, S_i/B_i , are the highest). The energy range of the fitted flux is then the central 90 per cent quantile of the true energy distribution.

STATE OF G20 SOURCES DURING NEUTRINO ARRIVAL TIMES

We provide example light curves and their bayesian block decomposition for the case of TXS 0506+056 in Figure A1.

SEDS

We show the SEDs for the 34 G20 sources in Figure A2. SEDs for excluded sources due to updated alert event criteria are displayed in Figure A3.

¹⁰ <https://github.com/icecube/skylh>

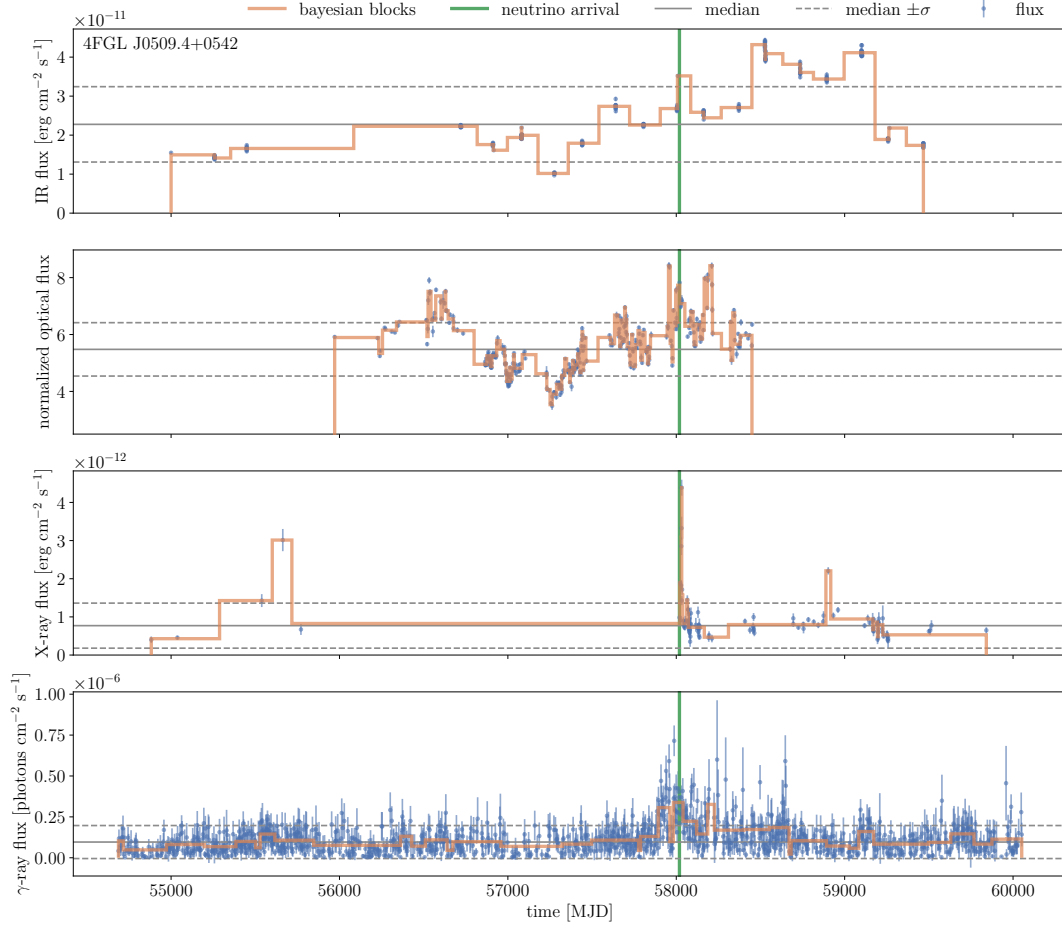


Figure A1. Light curves and their bayesian block decomposition for TXS 0506+056 in the IR, optical, X-ray, and γ -ray bands (top to bottom), where time is given in Modified Julian Date (MJD) format. We show the median flux as the horizontal solid grey line and the standard deviation as the horizontal dashed grey lines. The neutrino arrival time is indicated by the green vertical line. The orange histogram shows the bins identified by bayesian block decomposition. At the time of the neutrino arrival, the source was found to be in a flaring state in the IR, optical and γ -rays. In the X-ray band (1 keV), the flare begins right after the neutrino arrival time and is not identified as a coincident arrival.

This paper has been typeset from a \LaTeX file prepared by the author.

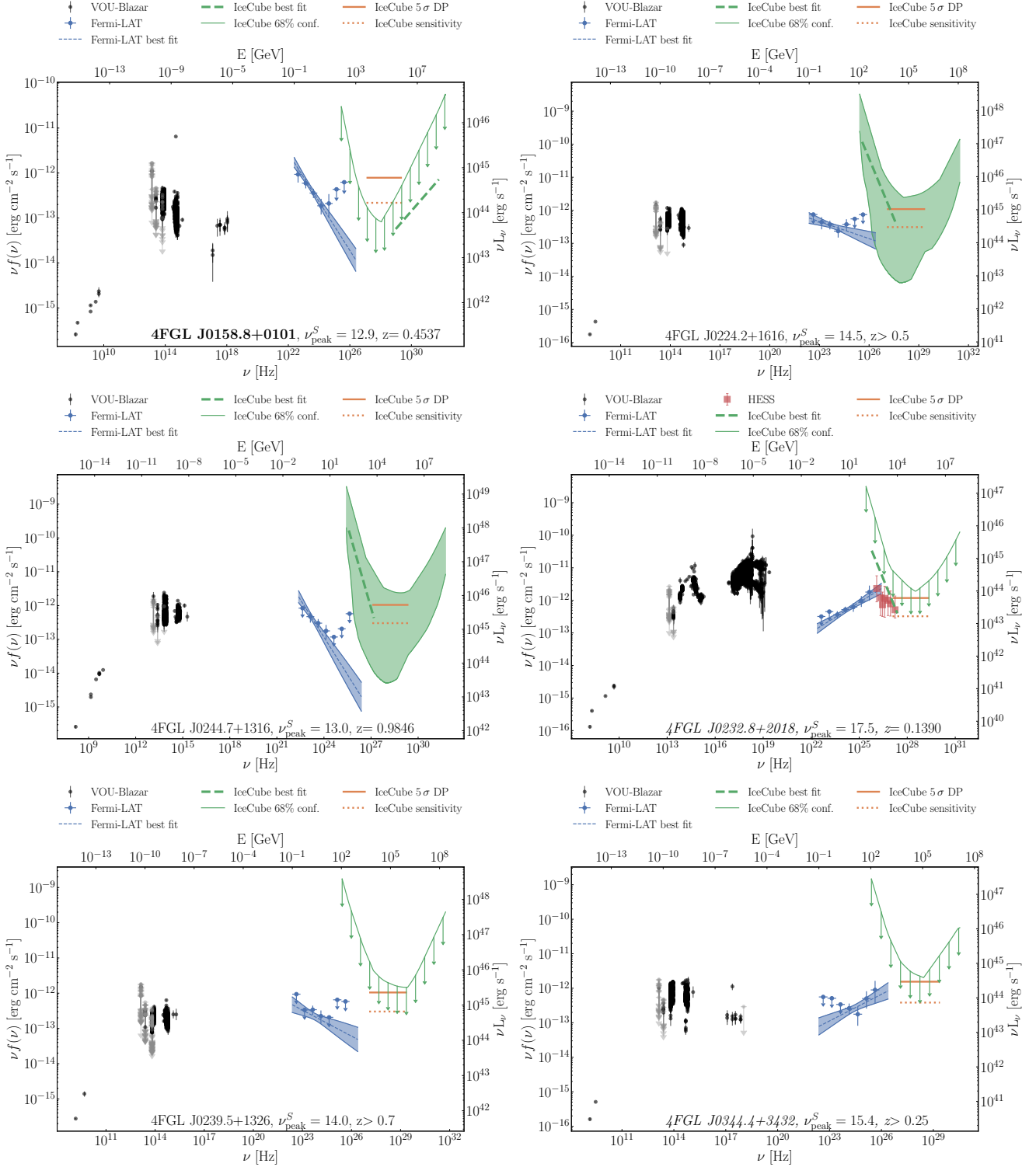


Figure A2. SEDs of all investigated objects. The black dots show the multi-wavelength data, and upper limits are displayed in grey. The blue dots display the best fit of the *Fermi*-LAT SED, and the blue bowtie indicates the uncertainties for the fitted gamma-ray flux. For two objects (4FGL J0232.8+2018 [3HSP J023248.5+20171] and 4FGL J0509.4+0542 [TXS 0506+056]) we include MAGIC (IceCube Collaboration et al. 2018b) and HESS (Costamante et al. 2018) data in red (uncorrected for extragalactic background light absorption). The solid (dashed) orange line shows the 5σ discovery potential (the sensitivity) for neutrino emission from Aartsen et al. (2020). The discovery potential (DP) is the flux (with an E^{-2} spectrum) necessary to detect the source with 5σ significance at 50 per cent confidence level. The sensitivity shows the 90 per cent confidence flux limit in case of no neutrino flux (also assuming an E^{-2} spectrum). The green line (band) shows the 68 per cent confidence limits (band) on the best-fit neutrino flux based on public IceCube data (IceCube Collaboration et al. 2021). If the best-fit neutrino flux was > 0 , we show it as a green dashed line. All neutrinos fluxes are single flavour (muon neutrino and antineutrino) fluxes. We list the observed ν_{peak}^S and the redshift. Masquerading sources are marked in bold, and sources where the extension of the γ -ray flux meets the 5σ discovery potential or the best-fit neutrino flux are marked in italics.

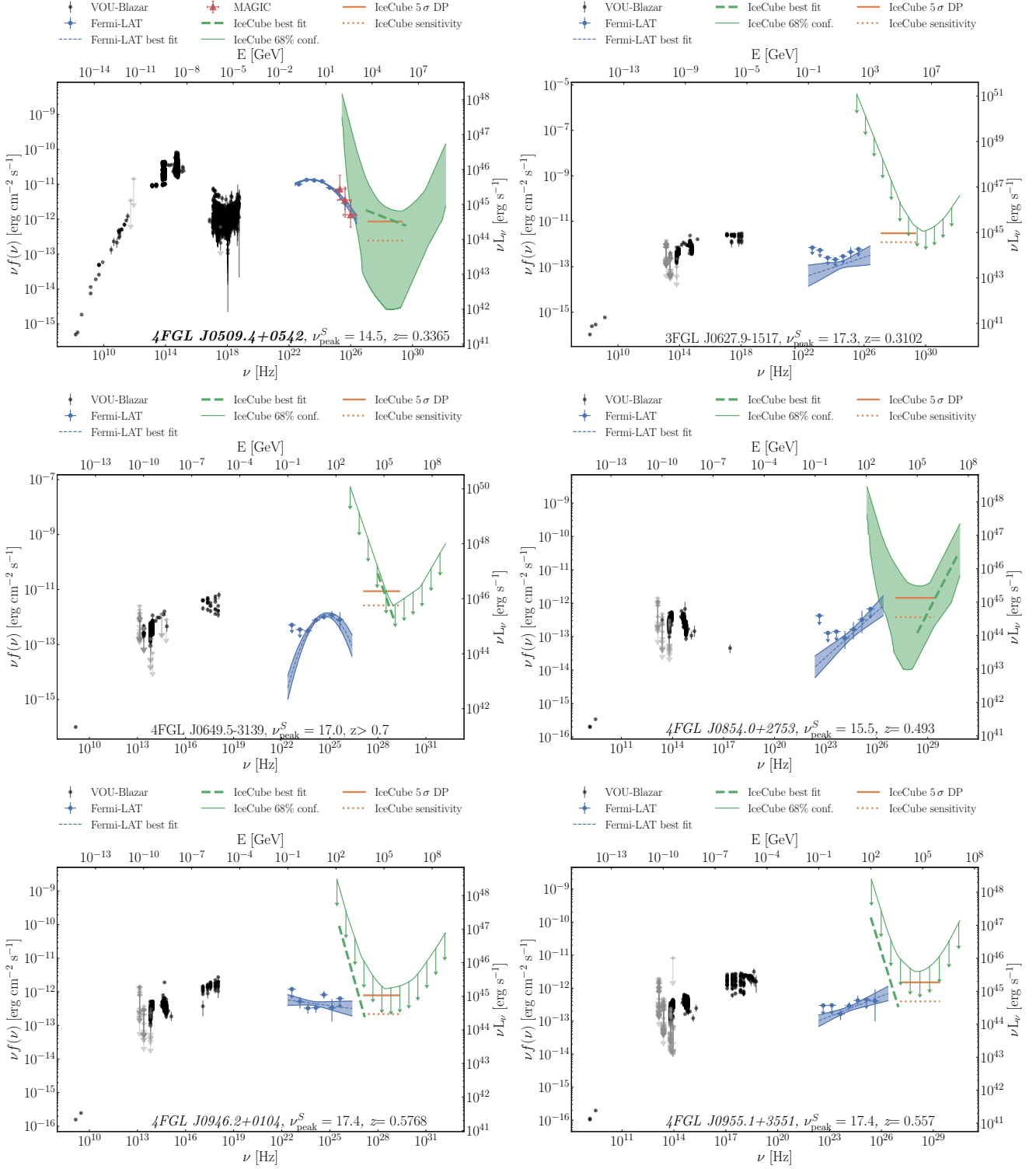


Figure A2. - Continued

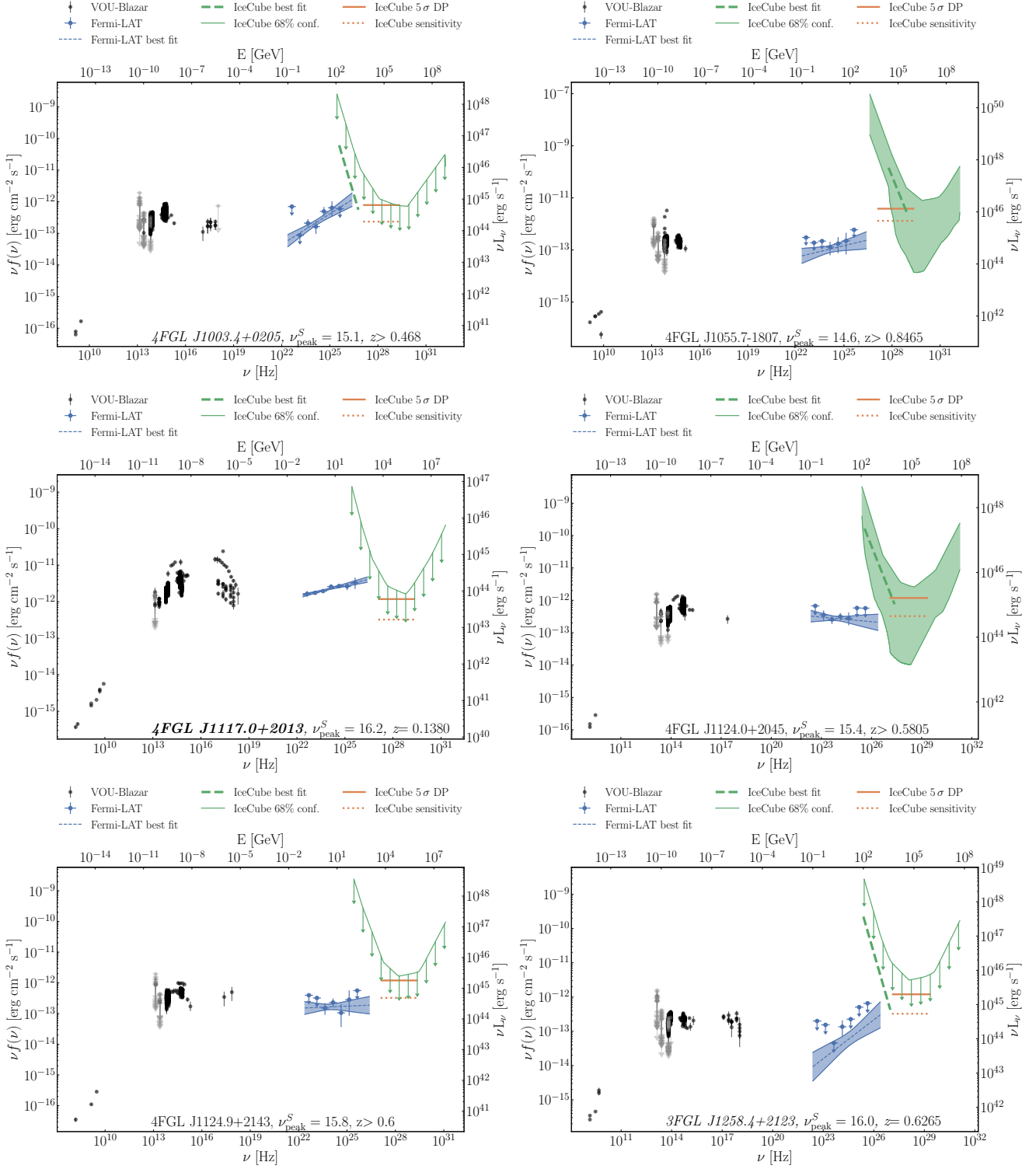


Figure A2. - Continued

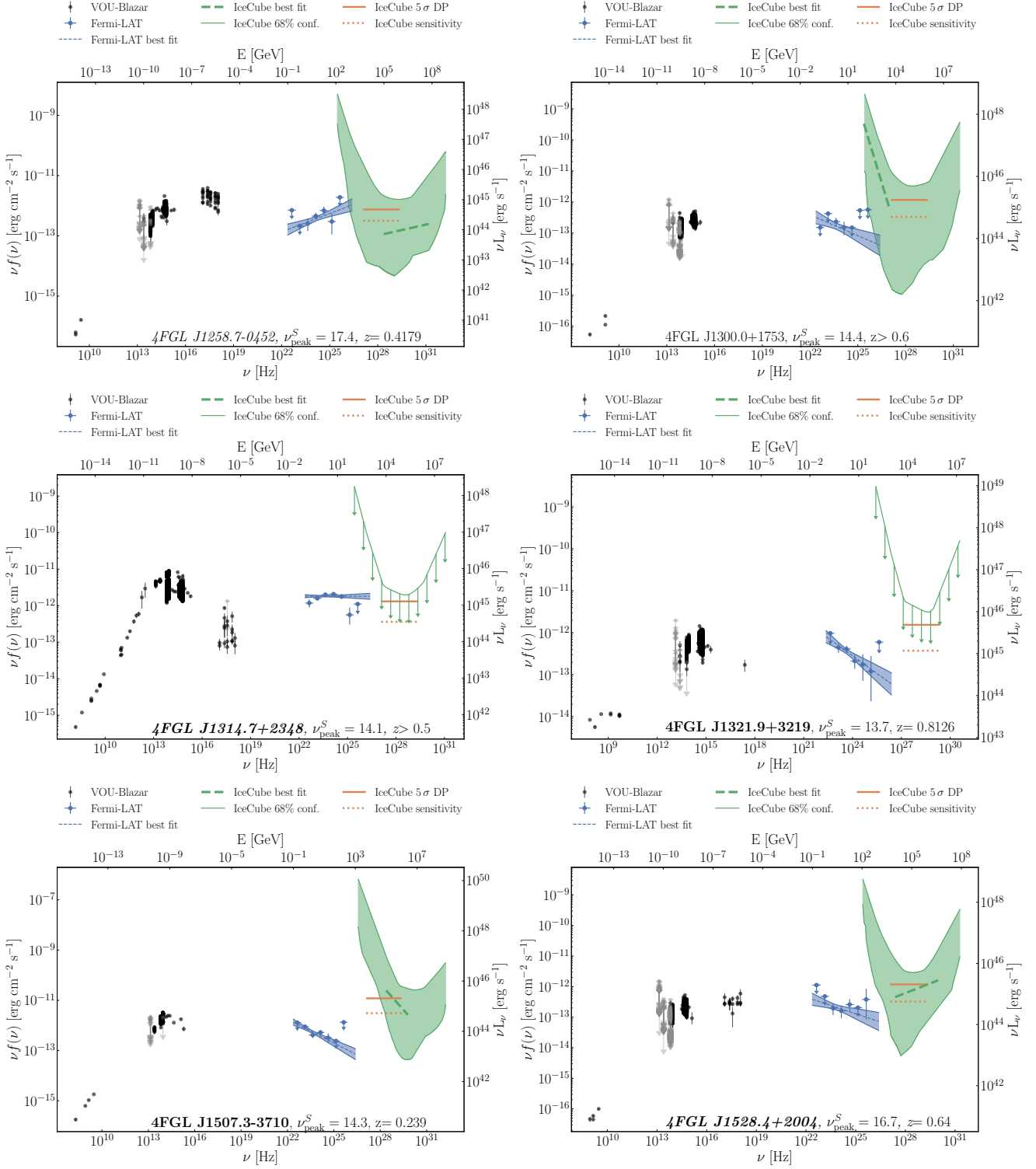


Figure A2. - Continued

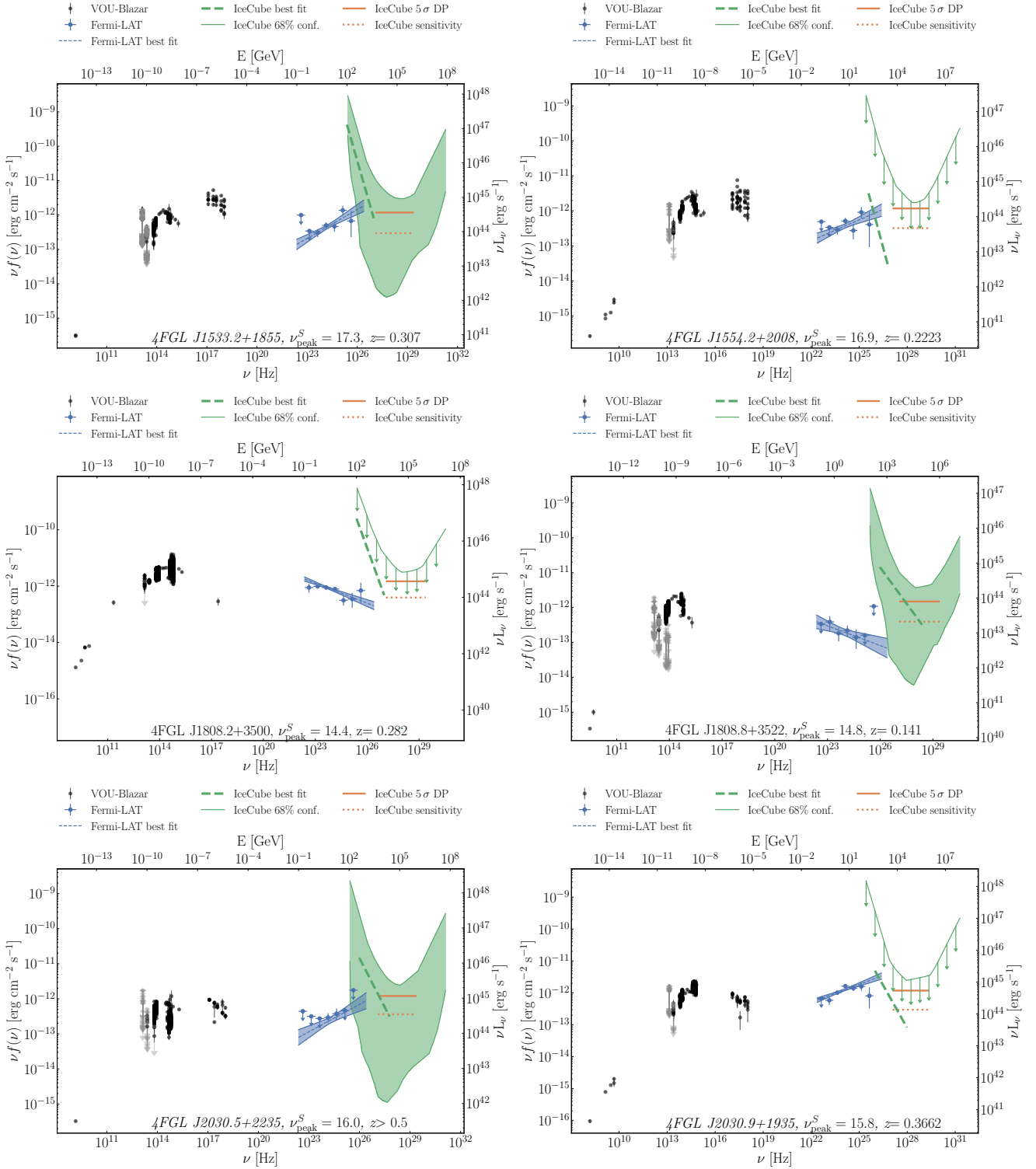


Figure A2. - Continued

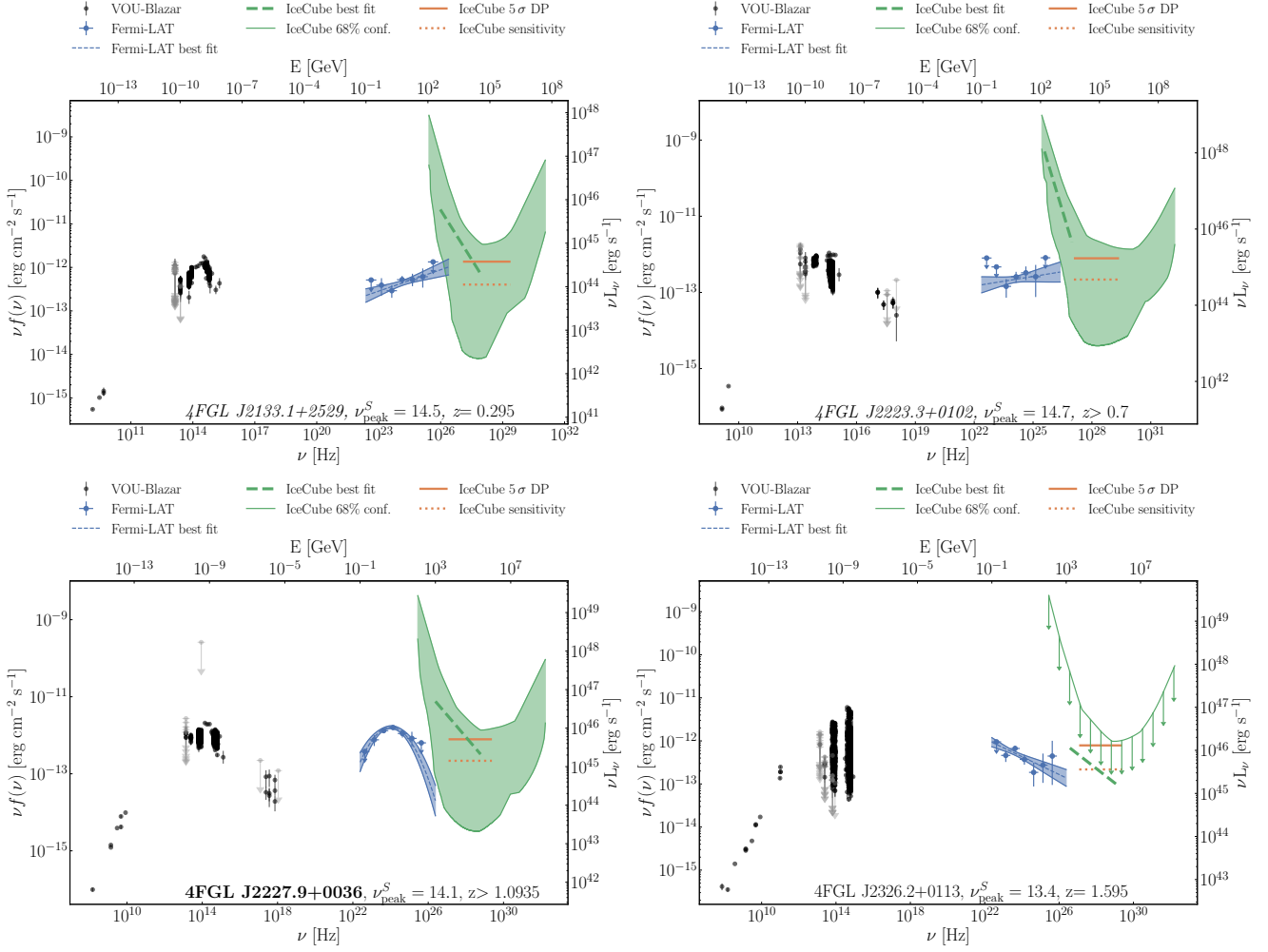


Figure A2. - Continued

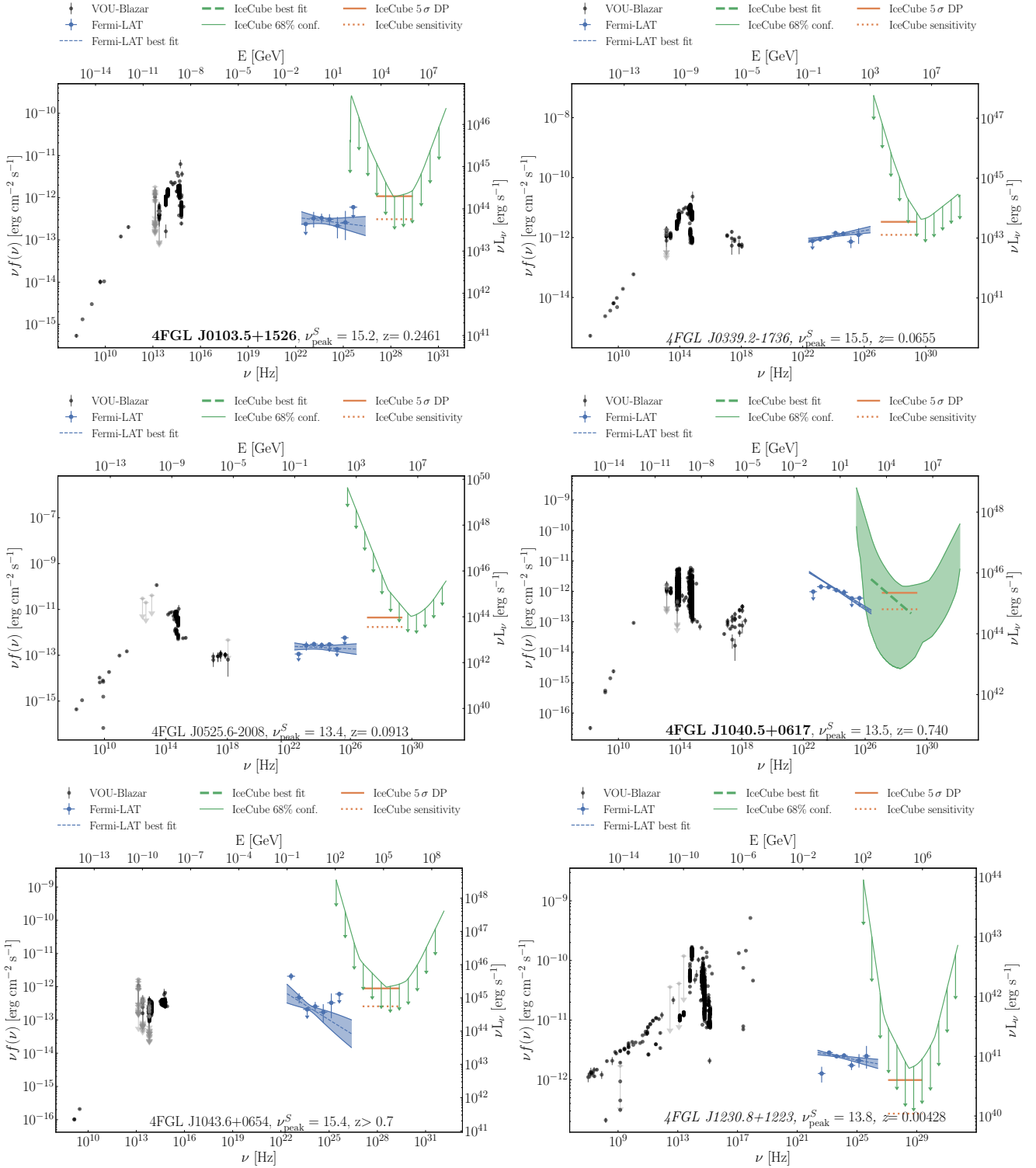


Figure A3. SEDs of all excluded objects. The black dots show the multi-wavelength data, and upper limits are displayed in grey. The blue dots display the best fit of the *Fermi*-LAT SED, and the blue bowtie indicates the uncertainties for the fitted gamma-ray flux. The solid (dashed) orange line shows the 5 σ discovery potential (the sensitivity) for neutrino emission from Aartsen et al. (2020). The discovery potential (DP) is the flux (with an E^{-2} spectrum) necessary to detect the source with 5 σ significance at 50 per cent confidence level. The sensitivity shows the 90 per cent confidence flux limit in case of no neutrino flux (also assuming an E^{-2} spectrum). The green line (band) shows the 68 per cent confidence limits (band) on the best-fit neutrino flux based on public IceCube data (IceCube Collaboration et al. 2021). If the best-fit neutrino flux was > 0 , we show it as a green dashed line. All neutrinos fluxes are single flavour (muon neutrino and antineutrino) fluxes. Masquerading sources are marked in bold, and sources where the extension of the γ -ray flux meets the 5 σ discovery potential or the best-fit neutrino flux are marked in italics.

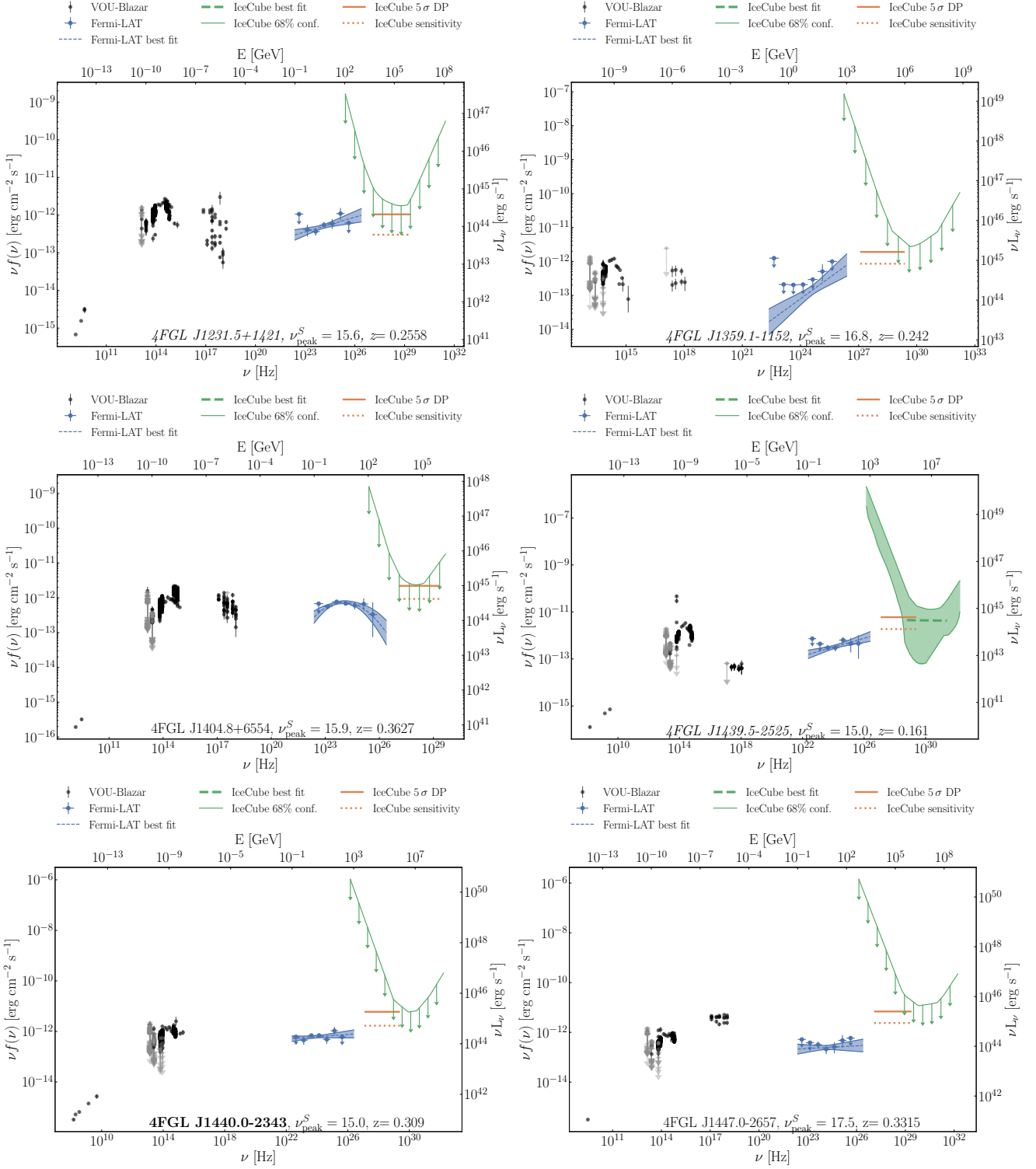


Figure A3. - Excluded Sources – Continued

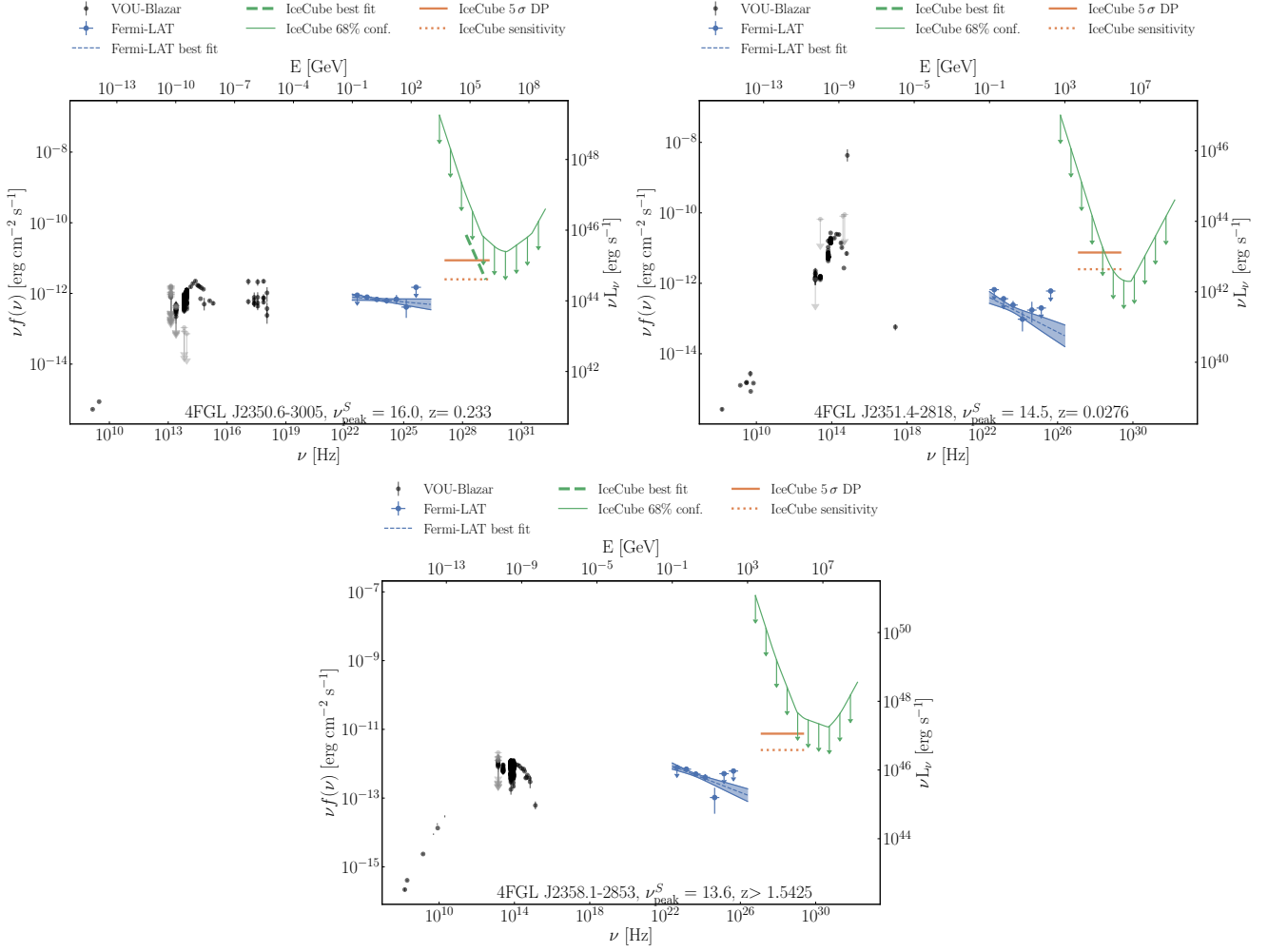
**Figure A3.** - Excluded Sources – Continued

Table A1. Overview of the time span and sampling of the light curve data.

4FGL Name	Name	IR			optical			X-ray		
		First	Last	N _{Obs}	First	Last	N _{Obs}	First	Last	N _{Obs}
4FGL J0158.8+0101	5BZU J0158+0101	55210.33	59415.80	213	58315.44	59883.23	265	-	-	-
4FGL J0224.2+1616	VOU J022411+161500	55221.32	59429.39	219	58301.48	59883.24	336	-	-	-
4FGL J0232.8+2018	3HSP J023248.5+20171	55223.83	59432.39	218	58301.48	59888.24	421	54683.60	59824.56	97
4FGL J0239.5+1326	3HSP J023927.2+13273	55223.30	59431.74	228	58336.49	59874.39	119	-	-	-
4FGL J0244.7+1316	CRATESJ024445+132002	55224.36	59432.92	247	58305.47	59889.25	249	-	-	-
4FGL J0344.4+3432	3HSP J034424.9+34301	55241.43	59450.43	237	58313.47	59889.24	326	-	-	-
4FGL J0509.4+0542	TXS 0506+056	55257.57	59467.56	246	58204.14	59889.25	279	54882.43	59841.30	108
3FGL J0627.9-1517	3HSP J062753.3-15195	55277.68	59490.70	287	58373.50	59882.42	111	-	-	-
4FGL J0649.5-3139	3HSP J064933.6-31392	55288.66	59499.59	352	-	-	-	56096.97	59026.75	12
4FGL J0854.0+2753	3HSP J085410.1+27542	55310.11	59520.36	230	58206.19	59882.51	159	-	-	-
4FGL J0946.2+0104	3HSP J094620.2+01045	55329.42	59545.45	230	58202.25	59881.46	284	56110.50	57572.08	10
4FGL J0955.1+3551	3HSP J095507.9+35510	55319.64	59529.38	272	58202.26	59889.49	342	56036.35	58900.05	35
4FGL J1003.4+0205	3HSP J100326.6+02045	55332.86	59545.71	226	58202.26	59888.46	223	56671.93	59558.89	4
4FGL J1055.7-1807	VOU J105603-180929	55354.95	59357.92	232	58244.19	59722.20	57	-	-	-
4FGL J1117.0+2013	3HSP J111706.2+20140	55344.64	59553.55	233	58202.27	59743.26	273	54941.55	56491.25	4
4FGL J1124.0+2045	3HSP J112405.3+20455	55345.96	59554.73	237	58202.29	59889.50	155	-	-	-
4FGL J1124.9+2143	3HSP J112503.6+21430	55345.83	59554.46	245	58235.22	59304.35	26	-	-	-
3FGL J1258.4+2123	3HSP J125821.5+21235	55366.21	59368.77	240	58235.23	58967.25	14	-	-	-
4FGL J1258.7-0452	3HSP J125848.0-04474	55205.27	59379.10	226	58203.31	59758.22	157	56327.21	57728.78	11
4FGL J1300.0+1753	3HSP J130008.5+17553	55370.44	59370.61	260	58202.31	59770.19	334	-	-	-
4FGL J1314.7+2348	5BZB J1314+2348	55371.11	59371.26	283	58202.31	59771.25	558	-	-	-
4FGL J1321.9+3219	5BZB J1322+3216	55366.08	59368.78	266	58202.35	59771.25	488	-	-	-
4FGL J1507.3-3710	VOU J150720-370902	55240.88	59422.10	139	-	-	-	-	-	-
4FGL J1528.4+2004	3HSP J152835.7+20042	55228.03	59408.52	256	58203.40	59812.22	268	58677.59	58760.32	6
4FGL J1533.2+1855	3HSP J153311.2+18542	55229.61	59414.27	321	58333.19	59390.25	21	55725.55	55942.06	5
4FGL J1554.2+2008	3HSP J155424.1+20112	55232.86	59418.45	287	58203.42	59853.14	400	57004.02	58767.17	8
4FGL J1808.2+3500	CRATESJ180812+350104	55278.31	59461.32	430	58204.43	59887.16	963	-	-	-
4FGL J1808.8+3522	3HSP J180849.7+35204	55278.57	59461.72	442	58245.49	59402.33	38	-	-	-
4FGL J2030.5+2235	3HSP J203031.6+22343	-	-	-	58230.50	59883.16	229	-	-	-
4FGL J2030.9+1935	3HSP J203057.1+19361	55321.31	59147.21	65	58211.51	59890.13	455	-	-	-
4FGL J2133.1+2529	3HSP J213314.3+25285	55342.35	59524.32	287	58277.48	59075.39	51	-	-	-
4FGL J2223.3+0102	3HSP J222329.5+01022	-	-	-	58262.47	59883.23	499	-	-	-
4FGL J2227.9+0036	5BZB J2227+0037	55345.27	59531.44	238	58263.48	59883.17	397	-	-	-
4FGL J2326.2+0113	CRATESJ232625+011147	55361.01	59542.22	233	58288.42	59889.23	276	-	-	-

Notes. Overview of the time span and the sampling of the light curve data used to calculate the FVs in the IR, optical, and X-ray bands for the sources that meet the newly revised criteria (Section 2). For each object, we list the dates of the first and last observation available and the number of observed data points N_{Obs}. All dates are given in MJD format.

Table A2. Overview of neutrino events and their coincidence with flares in different bands.

4FGL Name	Name	IR		optical		X-ray		γ -ray	
		flare	P_{BG}	flare	P_{BG}	flare	P_{BG}	flare	P_{BG}
4FGL J0158.8+0101	5BZU J0158+0101	✗	0.103	-	-	✗	0.0	-	-
4FGL J0224.2+1616	VOU J022411+161500	✗	0.1447	-	-	-	-	-	-
4FGL J0232.8+2018	3HSP J023248.5+20171	✗	0.0004	-	-	✓	0.3647	-	-
4FGL J0239.5+1326	3HSP J023927.2+13273	✗	0.1001	✗	0.0761	✗	0.0	✗	0.0
4FGL J0244.7+1316	CRATESJ024445+132002	✗	0.086	✗	0.0188	✗	0.0	✗	0.0
4FGL J0344.4+3432	3HSP J034424.9+34301	✗	0.2684	-	-	✗	0.0	-	-
4FGL J0509.4+0542	TXS 0506+056	✓	0.1813	✓	0.209	✗	0.0967	✓	0.0459
3FGL J0627.9-1517	3HSP J062753.3-15195	✗	0.0	-	-	✗	0.0	-	-
4FGL J0649.5-3139	3HSP J064933.6-31392	✓	0.4092	✗	0.0141	✗	0.0517	✗	0.0
4FGL J0854.0+2753	3HSP J085410.1+27542	✗	0.0	-	-	-	-	-	-
4FGL J0946.2+0104	3HSP J094620.2+01045	✗	0.0584	✗	0.1708	✗	0.0	-	-
4FGL J0955.1+3551	3HSP J095507.9+35510	✗	0.1996	✗	0.1798	✓	0.4555	-	-
4FGL J1003.4+0205	3HSP J100326.6+02045	✗	0.1649	✓	0.2492	✗	0.0	-	-
4FGL J1055.7-1807	VOU J105603-180929	✗	0.0	-	-	✗	0.0	-	-
4FGL J1117.0+2013	3HSP J111706.2+20140	✗	0.2804	-	-	✗	0.7629	✗	0.0
4FGL J1124.0+2045	3HSP J112405.3+20455	✗	0.0801	-	-	-	-	-	-
4FGL J1124.9+2143	3HSP J112503.6+21430	✗	0.1198	-	-	-	-	-	-
3FGL J1258.4+2123	3HSP J125821.5+21235	✗	0.0	-	-	✗	0.0	-	-
4FGL J1258.7-0452	3HSP J125848.0-04474	✓	0.167	-	-	✗	0.1965	-	-
4FGL J1300.0+1753	3HSP J130008.5+17553	✗	0.125	-	-	-	-	-	-
4FGL J1314.7+2348	5BZB J1314+2348	✗	0.295	✗	0.05	✗	0.0	✗	0.0
4FGL J1321.9+3219	5BZB J1322+3216	✗	0.0836	-	-	-	-	-	-
4FGL J1507.3-3710	VOU J150720-370902	✗	0.0	-	-	-	-	-	-
4FGL J1528.4+2004	3HSP J152835.7+20042	✗	0.0602	-	-	✗	0.0371	-	-
4FGL J1533.2+1855	3HSP J153311.2+18542	✗	0.0	-	-	✗	0.0	-	-
4FGL J1554.2+2008	3HSP J155424.1+20112	✗	0.0959	-	-	✗	0.0012	-	-
4FGL J1808.2+3500	CRATESJ180812+350104	✗	0.222	-	-	-	-	✗	0.0
4FGL J1808.8+3522	3HSP J180849.7+35204	✗	0.3084	-	-	✗	0.0	-	-
4FGL J2030.5+2235	3HSP J203031.6+22343	-	-	-	-	✗	0.4595	-	-
4FGL J2030.9+1935	3HSP J203057.1+19361	✗	0.286	-	-	✗	0.0	-	-
4FGL J2133.1+2529	3HSP J213314.3+25285	✗	0.0814	-	-	-	-	-	-
4FGL J2223.3+0102	3HSP J222329.5+01022	-	-	-	-	✗	0.0	-	-
4FGL J2227.9+0036	5BZB J2227+0037	✗	0.2049	-	-	✗	0.0	-	-
4FGL J2326.2+0113	CRATESJ232625+011147	✗	0.1996	✗	0.0417	✗	0.0	✗	0.0

Notes. Overview of all G20 sources meeting the revised criteria in Section 2 with information on their flaring state at the time of the neutrino arrival (✓ if yes, ✗ if no, - if no data was available) for the different bands. P_{BG} gives the chance probability of finding the source in a flaring state (fraction of the time a source was flaring vs. the whole observation time), with $P_{BG} = 0$ if there was no flare in the light curve. TXS 0506+056 is the only object found in a flaring state in several wavelengths during the neutrino arrival time.